Article

Molecular Cell

# Temperature-Responsive Competitive Inhibition of CRISPR-Cas9

## Graphical Abstract

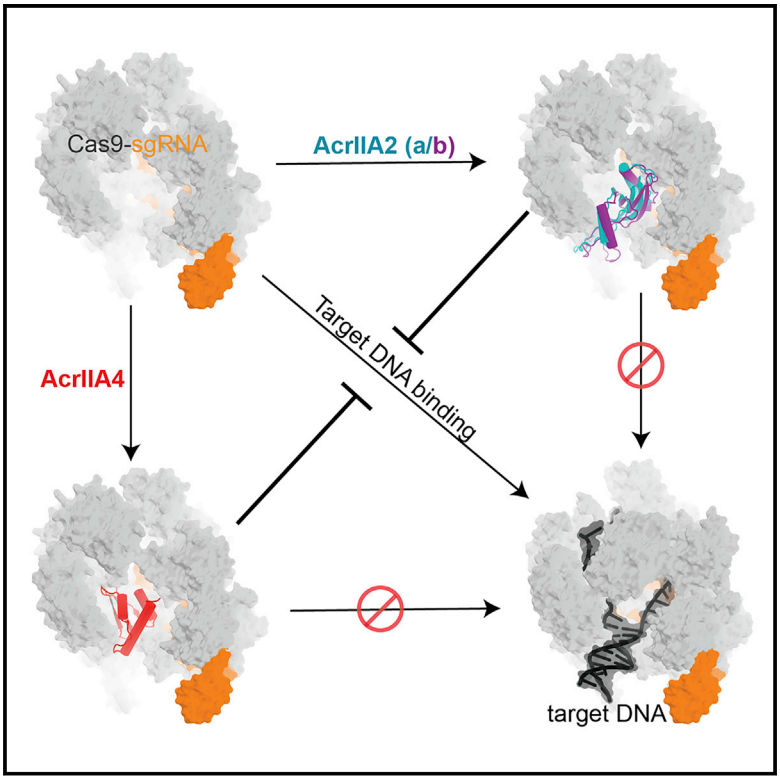


## Highlights

- Atomic cryo-EM structure of AcrIIA2- or AcrIIA2b-bound SpyCas9-sgRNA complex
- AcrIIA2 inhibitor family shows a convergent Cas9 inhibition mechanism with AcrIIA4
- AcrIIA2 exhibits a strong temperature-dependent anti-CRISPR activity

## Authors

Fuguo Jiang, Jun-Jie Liu, Beatriz A. Osuna, ..., Eva Nogales, Joseph Bondy-Denomy, Jennifer A. Doudna

## Correspondence

joseph.bondy-denomy@ucsf.edu (J.B.-D.), doudna@berkeley.edu (J.A.D.)

## In Brief

Jiang et al. report cryo-EM structures of type II-A anti-CRISPRs (AcrIIA2 and its homolog AcrIIA2b) bound to *S. pyogenes* Cas9, revealing a convergent inhibition mechanism between AcrIIA2 and AcrIIA4. The temperature-dependent differences between AcrIIA2 and AcrIIA2b provide an interesting condition-dependent variable that could be exploited for developing Cas9-based tools.

## Data Resource

6MCB
6MCC

Jiang et al., 2019, Molecular Cell *73*, 601–610
February 7, 2019 © 2018 Elsevier Inc.
https://doi.org/10.1016/j.molcel.2018.11.016

CellPress

Molecular Cell
Article

# Temperature-Responsive Competitive Inhibition of CRISPR-Cas9

Fuguo Jiang,[1,2,10] Jun-Jie Liu,[1,8,10] Beatriz A. Osuna,[6,10] Michael Xu,[3] Joel D. Berry,[6,7] Benjamin J. Rauch,[6,7] Eva Nogales,[1,3,5,8] Joseph Bondy-Denomy,[6,7,*] and Jennifer A. Doudna[1,2,3,4,5,8,9,11,*]
[1]Department of Molecular and Cell Biology, University of California, Berkeley, Berkeley, CA 94720, USA
[2]California Institute for Quantitative Biosciences, University of California, Berkeley, Berkeley, CA 94720, USA
[3]Department of Chemistry, University of California, Berkeley, Berkeley, CA 94720, USA
[4]Innovative Genomics Institute, Berkeley, CA 94704, USA
[5]Howard Hughes Medical Institute, Berkeley
[6]Department of Microbiology and Immunology, University of California, San Francisco, San Francisco, CA 94143, USA
[7]California Institute for Quantitative Biosciences, University of California, San Francisco, San Francisco, CA 94143, USA
[8]MBIB Division, Lawrence Berkeley National Laboratory, Berkeley, CA 94720, USA
[9]Gladstone Institutes, San Francisco, CA 94158, USA
[10]These authors contributed equally
[11]Lead Contact
*Correspondence: joseph.bondy-denomy@ucsf.edu (J.B.-D.), doudna@berkeley.edu (J.A.D.)
https://doi.org/10.1016/j.molcel.2018.11.016

## SUMMARY

**CRISPR-Cas immune systems utilize RNA-guided nucleases to protect bacteria from bacteriophage infection. Bacteriophages have in turn evolved inhibitory "anti-CRISPR" (Acr) proteins, including six inhibitors (AcrIIA1–AcrIIA6) that can block DNA cutting and genome editing by type II-A CRISPR-Cas9 enzymes. We show here that AcrIIA2 and its more potent homolog, AcrIIA2b, prevent Cas9 binding to DNA by occluding protein residues required for DNA binding. Cryo-EM-determined structures of AcrIIA2 or AcrIIA2b bound to *S. pyogenes* Cas9 reveal a mode of competitive inhibition of DNA binding that is distinct from other known Acrs. Differences in the temperature dependence of Cas9 inhibition by AcrIIA2 and AcrIIA2b arise from differences in both inhibitor structure and the local inhibitor-binding environment on Cas9. These findings expand the natural toolbox for regulating CRISPR-Cas9 genome editing temporally, spatially, and conditionally.**

## INTRODUCTION

Bacteriophages are the most abundant biological entity on the planet and impart strong selective pressure on their bacterial hosts. In addition to their innate defense systems, bacteria have also developed adaptive immunity known as CRISPR-Cas to recognize and destroy foreign nucleic acids in a sequence-specific manner (Barrangou and Marraffini, 2014; Hille and Charpentier, 2016; Marraffini, 2015; Marraffini and Sontheimer, 2010). CRISPR-Cas systems are classified into six diverse types (I–VI) (Koonin et al., 2017; Makarova et al., 2015) that use a CRISPR genomic sequence array to record genetic evidence of prior infections. Small RNA guides transcribed from the array, together with Cas nucleases, target and degrade phage DNA or RNA (Hale et al., 2009; Marraffini and Sontheimer, 2008; Wiedenheft et al., 2011).

To counteract CRISPR-Cas immunity, phages employ inhibitory proteins to inactivate CRISPR-Cas function in a sequence-independent manner (Bondy-Denomy et al., 2013; Sontheimer and Davidson, 2017). To date, >40 diverse anti-CRISPRs have been identified in phages, prophages, and mobile genetic elements (Borges et al., 2017). Notably, four distinct anti-CRISPR proteins that inhibit type II-A CRISPR-Cas9 (AcrIIA1–AcrIIA4) from *Listeria monocytogenes* prophages were identified along with three that inactivate type II-C Cas9 orthologs (AcrIIC1–3), representing the first identification of anti-CRISPR proteins in type II CRISPR-Cas systems (Pawluk et al., 2016; Rauch et al., 2017). More recently, AcrIIA5 and AcrIIA6 have also been discovered in *Streptococcus thermophilus* phages (Hynes et al., 2017, 2018). Two of these inhibitors, AcrIIA2 and AcrIIA4, possess a broad-spectrum host range by inhibiting the activity of *Streptococcus pyogenes* Cas9 (53% amino acid identity to *L. monocytogenes* Cas9) in bacterial and human cells, although the ability of AcrIIA2 to block Cas9 functions is weaker than that of AcrIIA4 (Rauch et al., 2017). AcrIIA4 can function as a gene editing "off-switch" in human cells by reducing off-target mutations (Shin et al., 2017), by limiting Cas9-mediated toxicity in hematopoietic stem cells (Li et al., 2018), and by halting dCas9-based epigenetic modifications (Liu et al., 2018). Additionally, AcrIIA2 and AcrIIA4 have been used to limit Cas9-mediated gene drives in yeast (Basgall et al., 2018), demonstrating wide-ranging utility for these proteins. Structural studies showed that AcrIIA4 acts as a DNA mimic and binds to the PAM-interacting motif of the Cas9 protein to prevent target DNA binding and cleavage (Dong et al., 2017; Shin et al., 2017; Yang and Patel, 2017). Biochemical work suggested that AcrIIA2 also prevented the Cas9-DNA interaction (Dong et al., 2017; Yang and Patel, 2017); however, the mechanism and structural basis of its inhibitory activity remained obscure.

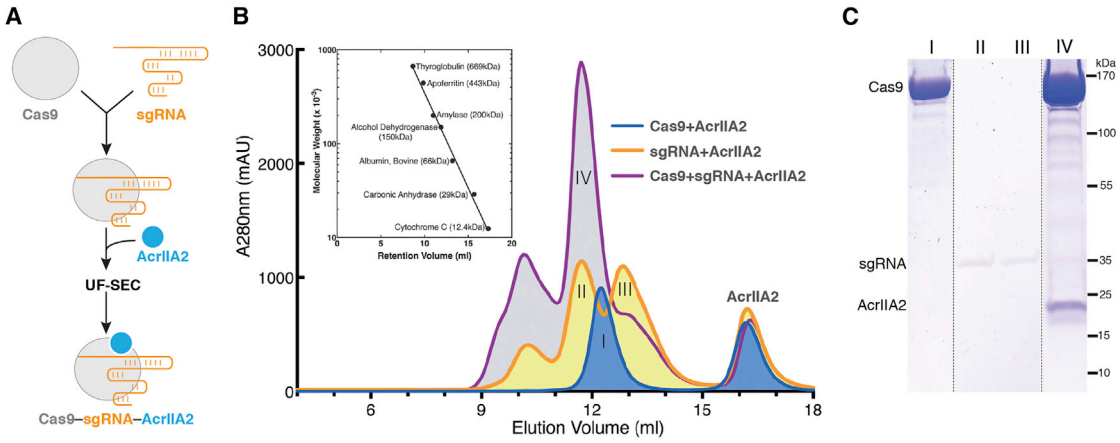


**Figure 1. AcrIIA2 Selectively Forms a Stable Complex with the sgRNA-Loaded *S. pyogenes* Cas9**

(A) Flow chart for reconstitution and isolation of the AcrIIA2-bound SpyCas9-sgRNA ternary complex using ultrafiltration combined with size-exclusion chromatography (UF-SEC).

(B) Size-exclusion chromatogram of SpyCas9-AcrIIA2 in the presence or absence of sgRNA. The inset represents the calibration curve obtained using standard molecular weight markers.

(C) Coomassie-stained polyacrylamide gel showing the co-purification of AcrIIA2 with sgRNA-bound SpyCas9.

To determine the mechanism of AcrIIA2-mediated Cas9 inhibition and to explore its utility as an effective "off-switch" for CRISPR-Cas9 regulation in genome editing applications, we determined a 3.4-Å-resolution cryo-EM structure of AcrIIA2 interacting with sgRNA-loaded SpyCas9. Additionally, we identified a homolog of AcrIIA2 (AcrIIA2b), encoded on an *L. monocytogenes* plasmid, which has more robust SpyCas9 inhibitory activity both *in vitro* and *in vivo*. A 3.9-Å cryo-EM structure of AcrIIA2b bound to SpyCas9 revealed a binding pocket similar to that observed in AcrIIA4 for blocking PAM recognition, which results in a more robust inhibition by AcrIIA2b relative to AcrIIA2. We show that temperature-dependent inhibition occurs *in vitro* and likely results from differences in the stability of the interaction with Cas9 at different temperatures. This work provides a comprehensive analysis of CRISPR-Cas9 functional interference mediated by the AcrIIA2 inhibitor family, but also provides a framework for future structure-based anti-CRISPR engineering and small peptide inhibitor design for precise and efficient control of Cas9-mediated genome editing.

## RESULTS

### Architecture of AcrIIA2 Bound to sgRNA-Loaded SpyCas9

AcrIIA2 is a type II-A anti-CRISPR commonly found in phages and prophages of *L. monocytogenes*, comprising 123 amino acids, that inhibits SpyCas9 both *in vitro* and *in vivo* (Basgall et al., 2018; Rauch et al., 2017; Yang and Patel, 2017). We first investigated at which step of CRISPR-Cas9 assembly AcrIIA2 inactivates Cas9 function. We performed size-exclusion chromatography (SEC) to test whether AcrIIA2 physically interacts with either SpyCas9 or sgRNA, or with the binary complex. Consistent with previous biochemical observations (Yang and Patel, 2017), AcrIIA2 can only form a stable complex with sgRNA-loaded SpyCas9, and no direct interaction occurs with either apo-SpyCas9 or sgRNA alone (Figure 1). This chromatographic profile of complex formation is similar to what has been observed for AcrIIA4 (Dong et al., 2017; Shin et al., 2017; Yang and Patel, 2017), indicating that AcrIIA2 has an interaction with SpyCas9 similar to that with AcrIIA4 and most likely binds to Cas9 at a region that is created upon sgRNA-triggered conformational rearrangement in Cas9 (Jiang et al., 2015).

In order to elucidate the detailed structural mechanism of AcrIIA2-mediated inhibition of Cas9 activity, we obtained images of the frozen-hydrated samples (Figure S1A) and solved the cryo-EM structure of SpyCas9-sgRNA-AcrIIA2 complex with an overall resolution of 3.4 Å (Figures 2, S1, and S2; Table 1). We observed electron density corresponding to the AcrIIA2 inhibitor protein with clear side-chain features (Figures 2A and 2B) that enabled atomic modeling of AcrIIA2 (Figure 2C). In contrast to the well-defined complex core region and the bound AcrIIA2, the HNH domain within SpyCas9 shows weaker density (Figures 2A), reflecting the intrinsic flexibility of this nuclease domain, as seen in prior structures (Anders et al., 2014; Jiang et al., 2015, 2016; Nishimasu et al., 2014).

In the refined atomic model of the SpyCas9-sgRNA-AcrIIA2 complex, the conformation of SpyCas9 resembles the pre-target-bound state rather than the dsDNA-bound state (Figure S3A–S3C). This suggests that AcrIIA2 binding blocks Cas9 conformational rearrangement, especially the HNH catalytic domain movement from the inactive state to the active state. Our *ab initio* modeling of the AcrIIA2-bound SpyCas9 complex demonstrated that AcrIIA2 sits within the nucleic-acid-binding channel that forms only upon sgRNA loading between the nuclease lobe (NUC) and helical recognition lobe (REC). This observation explains why sgRNA loading is critical for AcrIIA2 binding to Cas9. AcrIIA2 binds to the SpyCas9-sgRNA complex with 1:1 stoichiometry and at the same binding location as AcrIIA4 (Figures 2C and 2F). It is also worth noting that AcrIIA2

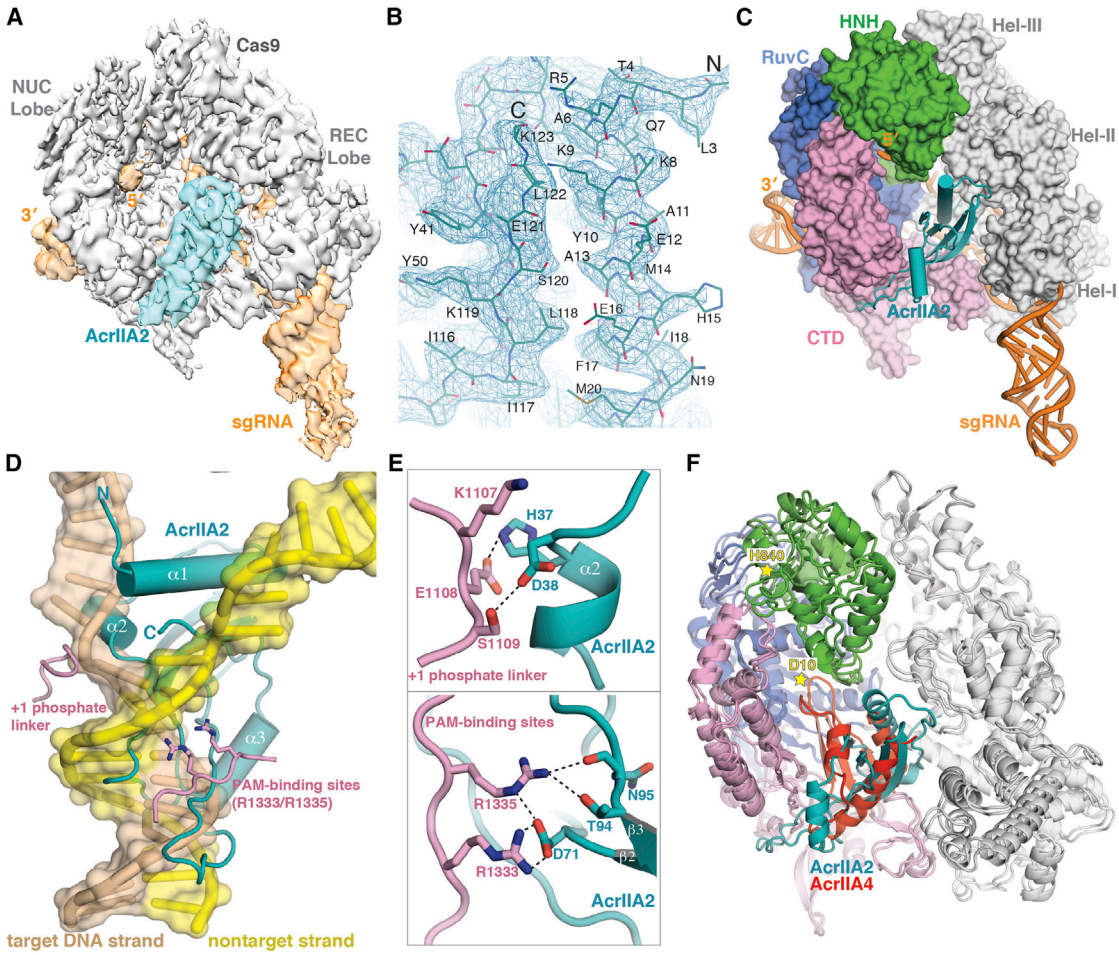


**Figure 2. Architecture of the *S. pyogenes* Cas9-sgRNA in Complex with AcrIIA2**

(A) Cryo-EM reconstruction of SpyCas9-sgRNA-AcrIIA2 at 3.4-Å resolution, segmented to highlight densities corresponding to SpyCas9 (gray) and AcrIIA2 (teal).

(B) Representative cryo-EM density for AcrIIA2 with the refined model superimposed.

(C) Surface representation of SpyCas9-sgRNA-AcrIIA2 ternary complex.

(D) Superimposition of AcrIIA2 (teal) with the dsDNA-bound SpyCas9 complex. For clarity, Cas9 is omitted except the target DNA strand and non-target strand.

(E) Close-up view showing how AcrIIA2 blocks target DNA binding by interacting with SpyCas9's PAM recognition residues (R1333/R1335) and +1 phosphate linker.

(F) Superposition with SpyCas9-sgRNA-AcrIIA4 structure (PDB ID 5VZL). Stars indicate the two catalytic residues (D10 of RuvC and H840 of HNH).

exists as a monomer in solution and maintains a single domain structure in the complex (Figures 1B and 2C).

The structure of AcrIIA2 is a mixed α+β fold, composed of a bent four-stranded antiparallel β sheet with a β4β1β3β2 arrangement, flanked by two helices, one on each side (Figures S4A–S4C). Notably, this topology of AcrIIA2 (α1α2β1β2β3α3β4) is distinct from that of AcrIIA4 (α1β1β2β3α2α3) and any other reported anti-CRISPR structures (Figures S4H–S4J). AcrIIA2 is structurally similar to aspartate-kinase chorismate-mutase tyrA (ACT) (Figure S4D), a regulatory domain found in a variety of proteins that exhibits low sequence conservation and high functional divergence from AcrIIA2 (Grant, 2006).

## AcrIIA2 Directly Blocks Target DNA Binding

Based on the cryo-EM structure of the AcrIIA2-bound SpyCas9 complex, we analyzed the detailed interactions between Cas9 and AcrIIA2 (Table S1). Superposition of the AcrIIA2-bound SpyCas9 structure onto the dsDNA-bound SpyCas9 structure reveals that AcrIIA2 is anchored into the PAM-duplex-interacting cleft to preclude target DNA binding to Cas9 (Figure 2D). Close inspection shows that AcrIIA2 likely makes an elaborate intermolecular hydrogen bonding network with the PAM-recognition site (R1333 and R1335) located in Cas9's C-terminal domain, primarily through the side chains of D71 and T94 and the main chain of N95 (Figures 2D and 2E). Consistent with this observation, the electrostatic potential distribution of AcrIIA2 reveals a highly negative pocket for interaction with the electropositive PAM-recognition site (Figure S4B). In addition, the surrounding residues S1136 and S1338, which are important for recognition of the PAM-proximal DNA duplex in the dsDNA-bound complex, are instead recognized by residues D96 and D60 in the AcrIIA2-bound structure (Figure S4A and Table S1). Given the

**Table 1. Cryo-EM Data Collection, 3D Reconstruction, and Model Refinement; Related to Figures 2 and 5**

| Data Collection | SpyCas9-sgRNA-AcrIIA2 | SpyCas9-sgRNA-AcrIIA2b |
|---|---|---|
| Grid | CF-2/2-4C-T (Protochips) | CF-2/2-4C-T (Protochips) |
| EM | Titan Krios 300 kV, K2 Gatan Summit | Titan Krios 300 kV, K2 Gatan Summit |
| Pixel size (Å) | 0.83 | 1.15 |
| Defocus range (μm) | −0.5 to −2.3 | −0.7 to −2.5 |
| Defocus determination | CTFFIND4 | CTFFIND4 |
| Particles picked | EMAN and Gautomatch | Gautomatch |
| Reconstruction (CryoSPARC) | | |
| Accuracy of rotations (°) | 1.87 | 2.035 |
| Accuracy of transitions (pixel) | 1.150 | 1.393 |
| Final resolution (Å) | 3.4 | 3.9 |
| Refinement (Phenix) | | |
| Map CC (entire box) | 0.793 | 0.798 |
| Map CC (around atoms) | 0.776 | 0.791 |
| RMSD | | |
| Bond lengths (Å) | 0.01 | 0.01 |
| Bond angles (°) | 1.09 | 1 |
| Ramachandran Plot | | |
| % favored | 92.65 | 91.48 |
| % allowed | 7.22 | 8.52 |
| % outliers | 0.13 | 0.00 |
| Molprobity | | |
| Clashscore | 5.67 | 6.05 |
| Accession Numbers | | |
| EMDB | 9066 | 9067 |
| PDB | 6MCB | 6MCC |

fact that PAM recognition is the first and key step for target DNA binding and unwinding (Sternberg et al., 2014), it is evident that interfering with the PAM-binding sites deployed by AcrIIA2 (as also seen in AcrIIA4) is an effective means to abolish Cas9-mediated target DNA binding and cleavage activities. To test whether PAM-recognition blockage confers SpyCas9 inhibition by AcrIIA2, we generated single (D71A) or double mutations (T94A/N95A) of AcrIIA2 residues involved in intermolecular contacts with the PAM-recognition site (R1333 and R1335) and analyzed their impact on inhibition of SpyCas9's *in vivo* DNA targeting activity. These mutations reduced phage survival in the presence of AcrIIA2 with D71A showing essentially complete loss of Cas9 inhibition (Figure 3A). This finding is consistent with *in vivo* evidence showing the loss of gene drive inhibition by unbiased alanine scanning mutagenesis of AcrIIA2 (D65A/D71A) (Basgall et al., 2018).

In addition to interactions with the PAM-binding site, AcrIIA2 makes extensive contacts with the helical domain I and II and the other parts of the C-terminal domain from SpyCas9 (Table S1). Specifically, residues H15, N19, E26, and T28 in the N-terminal α1-α2 of AcrIIA2 make hydrophilic interactions with the helical domain I and domain II. Moreover, the side chains of H37 and D38 of the bound AcrIIA2 interact with the phosphate lock loop (K1107–S1109) located in SpyCas9's PAM-interacting domain (Figures 2D and 2E). Previous structural studies indicated that this phosphate lock loop is critical for target DNA unwinding at +1 phosphate on the target DNA strand immediately upstream of the PAM motif (Anders et al., 2014). Superimposing dsDNA-bound and AcrIIA2-bound SpyCas9 reveals that AcrIIA2's α1 helix wedges between the target strand and nontarget DNA strand, whereas α2 helix penetrates the interface between +1 phosphate lock loop and target DNA strand (Figure 2D). These structural observations indicate that AcrIIA2 binding may also disrupt the target DNA unwinding activity of CRISPR-Cas9 in addition to blocking DNA binding. Indeed, mutational substitution of these residues (D38A/D40A) demonstrated a large reduction in effectiveness of AcrIIA2 as a Cas9 gene drive inhibitor (Basgall et al., 2018). Apart from these structural features, it is also noteworthy that AcrIIA2 does not interfere with the RuvC active site as observed in AcrIIA4-bound structure (Figure 2F).

We tested and confirmed that AcrIIA2 abrogates SpyCas9-DNA binding by performing gel shift competition assays. Wild-type SpyCas9-sgRNA was used together with 10 mM EDTA to prevent target DNA cleavage. As anticipated, the competition binding experiment with AcrIIA2 and target DNA added simultaneously to SpyCas9-sgRNA resulted in an attenuation or elimination of the dsDNA-bound SpyCas9-sgRNA ternary complex in a concentration-dependent manner (Figures 3B and S5). Furthermore, AcrIIA2 showed a weak competitive binding effect compared to AcrIIA4 (Figures S6A and S6B), indicating that AcrIIA2 binds sgRNA-loaded SpyCas9 with lower affinity than AcrIIA4. Consistent with this, AcrIIA4 can replace AcrIIA2 from the pre-formed anti-CRISPR complex by gel filtration analysis (Figures S6D and S6E), but not vice versa. Notably, neither AcrIIA2 nor AcrIIA4 bound to dsDNA-bound SpyCas9 (Figures 3B and S6C), suggesting that these proteins work *in vivo* by binding Cas9 before the DNA search process is completed (Shin et al., 2017).

## AcrIIA2 Is a Less Effective Inhibitor Than AcrIIA4

Structural comparison reveals that binding of AcrIIA2 or AcrIIA4 to sgRNA-loaded SpyCas9 results in a similar conformational change within SpyCas9 (Figure 2F). Moreover, AcrIIA2 sits in the same DNA-binding cavity as AcrIIA4, although they do not bear sequence or structural similarity. In particular, the local environment of AcrIIA2 involved in blocking the PAM-recognition site is almost identical to that of AcrIIA4, except for the lack of two bulky aromatic amino acids (Y41 and Y67 in AcrIIA4) (Figures S4A and S4H). Notably, residue Y67 of AcrIIA4 participates in the hydrogen bond network within the PAM-recognition site of SpyCas9, while Y41 forms hydrophobic and van der Waals interactions. We speculate that lack of these bulky hydrophobic residues may result in the lower effectiveness of AcrIIA2-mediated Cas9 inhibition as seen *in vivo*.

We then compared the Cas9-inhibitory activity of AcrIIA2 and AcrIIA4 by *in vitro* DNA cleavage assay. Previous *in vivo* studies showed that AcrIIA4 can completely inactivate Cas9 function,

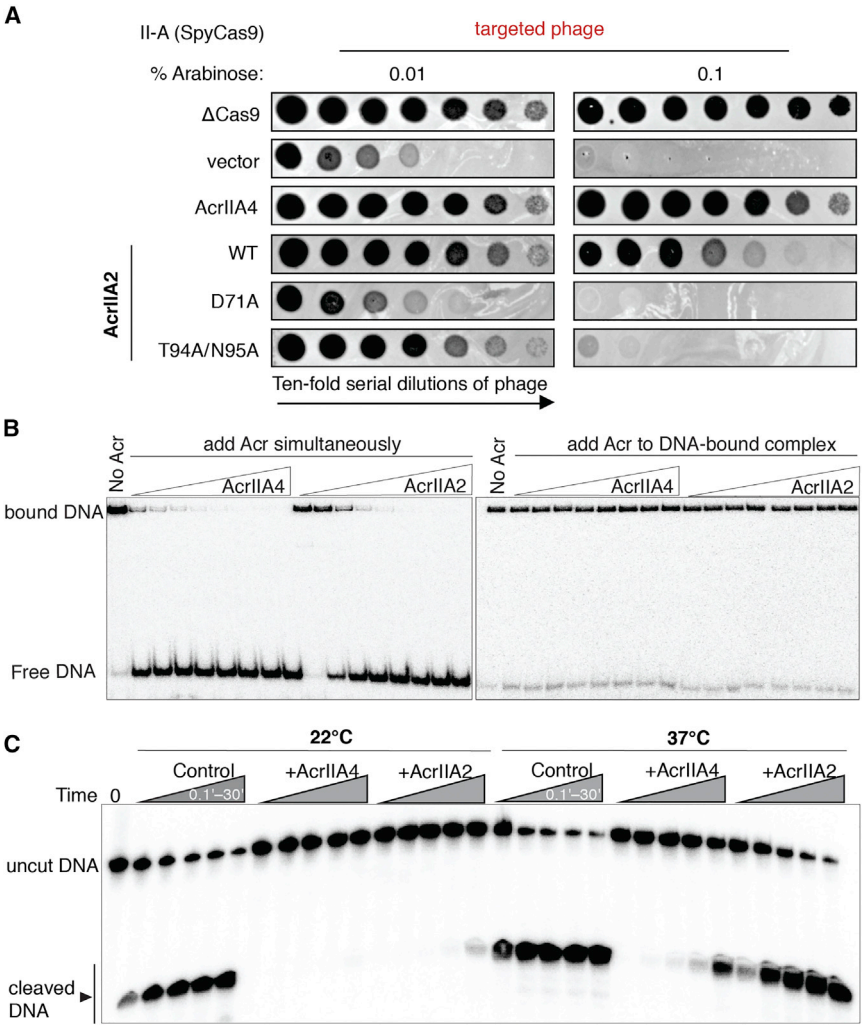


**Figure 3. AcrIIA2 Is a Much Less Effective Inhibitor Compared to AcrIIA4**

(A) Phage-plaquing experiment where *P. aeruginosa* JBD30 phage is titrated in 10-fold dilutions (black circles) on a lawn of *P. aeruginosa* (hazy background) expressing the indicated anti-CRISPR proteins and intermediate (0.01% arabinose) or high (0.1% arabinose) levels of a type II-A CRISPR-Cas9 system programmed to target phage DNA. Plaquing of *P. aeruginosa* phages targeted by SpyCas9 in the presence of AcrIIA2 mutants reveals a nearly complete inactivation of AcrIIA2's inhibitory effect on SpyCas9 by mutation of D71A.

(B) Competition EMSA assays showing that AcrIIA2 efficiently competes with target DNA for binding to SpyCas9-sgRNA complex (left), but not the pre-formed DNA-bound complex (right).

(C) Radiolabeled cleavage assays conducted using purified SpyCas9-sgRNA complex to assess AcrIIA2 capacity for inhibiting cleavage of both target and non-target DNA strands by SpyCas9 at room temperature and normal body temperature.

whereas AcrIIA2 only partially blocks Cas9 activity (Rauch et al., 2017). In line with this finding that AcrIIA2 and AcrIIA4 inhibit Cas9 function to different extents, *in vitro* experiments demonstrated that both anti-CRISPR proteins inhibit SpyCas9 enzymatic cleavage activity in a dose-dependent manner (Figures 3C and S5), with AcrIIA2 exhibiting a slightly weaker Cas9 inhibition compared to AcrIIA4 at room temperature (22°C). With large stoichiometric excess of inhibitors over SpyCas9, both AcrIIA2 and AcrIIA4 could fully block Cas9 function (Figures S5A, S5B, S5E, and S5F), in contrast with previous *in vivo* observations that AcrIIA2 only partially blocks Cas9 function in *E. coli* and human cells. To resolve this contradiction, we measured AcrIIA2- and AcrIIA4-mediated Cas9 cleavage inhibition at body temperature (37°C). While both inhibitors displayed a substantially decreased level of Cas9 inhibition compared to that observed at lower temperature (Figure 3C), AcrIIA2 failed to inhibit Cas9 even at extreme excess levels (1,000:1) (Figures S5G and S5H). By contrast, a large excess of AcrIIA4 (100:1) can lead to a complete loss of SpyCas9 cleavage activity (Figures S5C and S5D). Addition of urea to these reactions showed that AcrIIA2-mediated SpyCas9 inhibition is more susceptible to urea-induced denaturation (Figure S7A). Together with results from heat-induced denaturation of Cas9 inhibitors (Figure S7C), these data indicate that the AcrIIA2-Cas9 interaction possesses lower thermal stability than the AcrIIA4-Cas9 interaction, which could potentially limit its adoption in control of Cas9-based genome editing.

## Identification of AcrIIA2 Homologs with Enhanced Inhibition Activity

Because of the relative inability of the AcrIIA2 protein to inhibit SpyCas9 at human body temperature, we considered whether homologs of *acrIIA2* might possess enhanced inhibition activity against SpyCas9. Homologs of *acrIIA2* are found in prophages, phages, plasmids, and mobile islands within the *Listeria* genus. We identified two distinct sequence families, denoted AcrIIA2b and AcrIIA2c, which possess ~35% and ~50% sequence identity, respectively, to the original protein, AcrIIA2 (which corresponds to AcrIIA2a.1) (Figures 4A and S3G). To test the function of identified homologs, we established an assay in the bacterium *Pseudomonas aeruginosa* in which a chromosomal copy of SpyCas9 (arabinose-inducible) is programmed to target a *P. aeruginosa* phage, JBD30 (Figure 4B). Candidate *acrIIA2* orthologs were expressed from a plasmid (IPTG-inducible), allowing independent titration of the SpyCas9-sgRNA complex to assess anti-CRISPR strength.

Cas9-sgRNA function was subsequently assayed at three different levels of induction, revealing an increase in phage targeting as the effector concentration increased (Figure 4C). The expression of AcrIIA4 yields robust inhibition of Cas9-based phage targeting at all induction levels of Cas9, while AcrIIA2 provides limited activity under the strongest Cas9 induction conditions but functioned well at lower levels of Cas9 (Figure 4C).

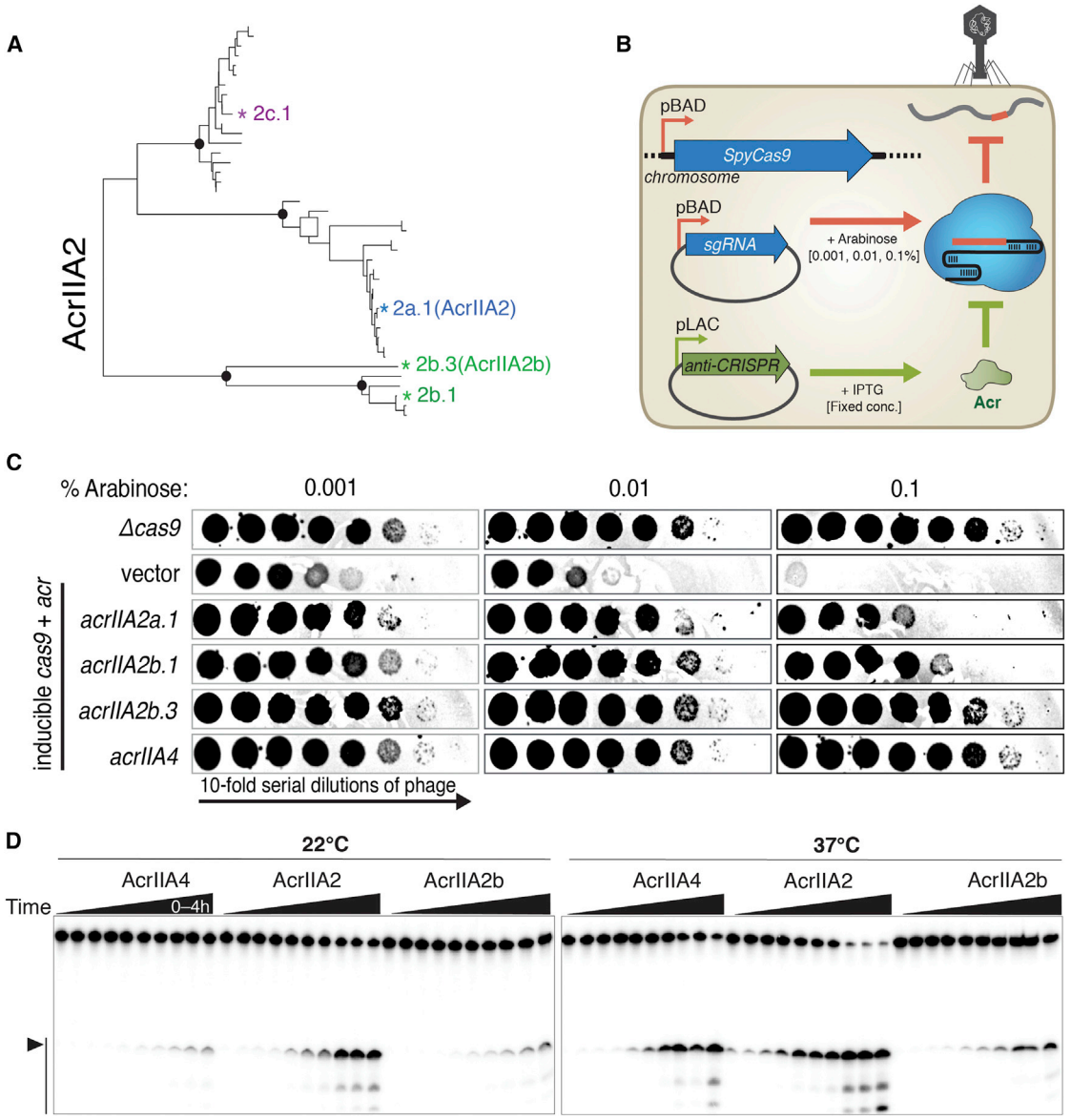


**Figure 4. Identifying AcrIIA2b.3 as a Potent SpyCas9 Inhibitor**

(A) Phylogenetic tree of the protein sequences of AcrIIA2 homologs.

(B) Schematic of the *P. aeruginosa* heterologous type II-A system utilized in (C), where phage is titrated in 10-fold dilutions (black circles) on a lawn of *P. aeruginosa* (white background) expressing the indicated anti-CRISPR proteins and low (0.001%), intermediate (0.01%), or high (0.1% arabinose) levels of SpyCas9-sgRNA programmed to target phage DNA.

(D) *In vitro* DNA cleavage inhibition assay shows AcrIIA2b.3 has the least temperature-dependent inhibitory activity.

Given the observed inefficiency of AcrIIA2 compared to AcrIIA4 in previous *E. coli* and human cell experiments (Rauch et al., 2017), it seems that this high level of Cas9-sgRNA induction mimics those experiments. Interestingly, two homologs from the AcrIIA2b family (AcrIIA2b.1 and AcrIIA2b.3) showed significantly stronger inhibition of SpyCas9 activity in comparison to AcrIIA2a, with AcrIIA2b.3 performing as well as AcrIIA4 (Figure 4C). Of note, expression of a protein from the AcrIIA2c family was toxic in *P. aeruginosa* and thus not pursued further. AcrIIA2b.1 did not express in *E. coli*, and therefore we chose AcrIIA2b.3 (henceforth referred to as AcrIIA2b), a protein encoded by a *Listeria* plasmid, for further biochemical analysis.

AcrIIA2b protein inactivates SpyCas9 function in a similar fashion to AcrIIA2 through direct interaction with sgRNA-loaded SpyCas9 (data not shown). We next examined the extent to which AcrIIA2b can suppress SpyCas9-mediated DNA cleavage *in vitro*. In excellent agreement with our *in vivo* results, AcrIIA2b displays more robust inhibitory capacity against SpyCas9 activity than AcrIIA2 at both room temperature and body temperature (Figure 4D). Importantly, the inhibition exhibited by AcrIIA2b at all

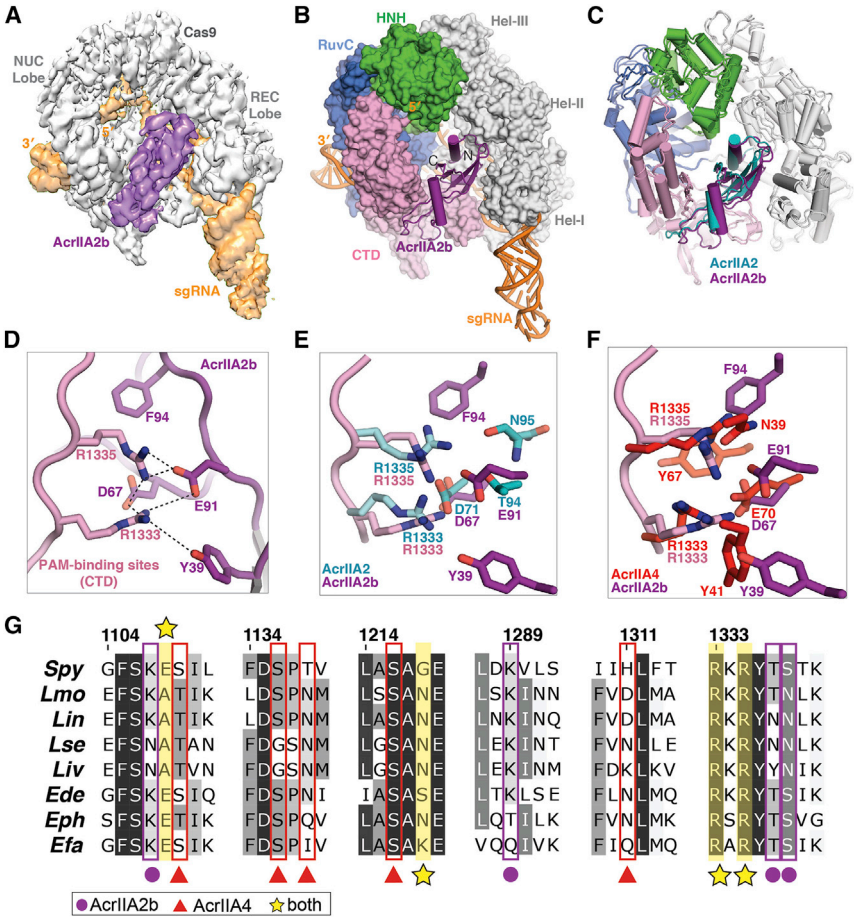


**Figure 5. AcrIIA2b Bears a Similar Interaction Network to AcrIIA4 for PAM-Recognition Interference**

(A) Cryo-EM reconstruction of the AcrIIA2b-bound SpyCas9.

(B) The atomic model of SpyCas9-sgRNA-ArcrIIA2b. AcrIIA2b (purple) and sgRNA (orange) are shown in ribbon diagram, and SpyCas9 is displayed as surface representation.

(C) Structural comparison of AcrIIA2- and AcrIIA2b-bound SpyCas9-sgRNA complex structures.

(D) Zoomed-in view of AcrIIA2b-SpyCas9 interaction at the PAM-recognition site.

(E and F) Overlay of AcrIIA2b PAM-interference pocket with that of AcrIIA2 (E) and that of AcrIIA4 (F).

(G) Alignment of Cas9 protein sequences denoting key residues that interact with the indicated anti-CRISPR proteins. Abbreviations: *Spy*, *Streptococcus pyogenes*; *Lmo*, *Listeria monocytogenes*; *Lin*, *Listeria innocua*; *Lse*, *Listeria seeligeri*; *Liv*, *Listeria ivanovii*; *Ede*, *Enterococcus devriesei*; *Eph*, *Enterococcus phoeniculicola*; *Efa*, *Enterococcus faecalis*.

tested conditions was similar to, if not better than, that exhibited by AcrIIA4 (Figure 4D). Competitive binding assays showed that AcrIIA2b competes with target DNA for binding to SpyCas9 when added to the enzyme simultaneously (Figure S6A), while preincubation of SpyCas9 with target DNA prevents engagement with AcrIIA2b (Figure S6C). Notably, the AcrIIA2b protein shows a greater affinity for SpyCas9 ($K_{D,app}$ = 230 nM) compared to AcrIIA2 ($K_{D,app}$ = 512 nM), whereas AcrIIA4 shows a comparable affinity ($K_{D,app}$ = 78 nM) to target DNA ($K_{D,app}$ = 26 nM) (Figure S6B). Taken together, these biochemical data indicate that AcrIIA2b recognizes the same binding site as AcrIIA2 in the SpyCas9-sgRNA binary complex and thereby prevents target DNA recognition and cleavage.

## Structure of AcrIIA2b-Bound SpyCas9 Reveals a Distinct Interaction Network for PAM-Recognition Interference

To determine the underlying structural basis for AcrIIA2b-mediated SpyCas9 inhibition, we determined the cryo-EM structure of the SpyCas9-sgRNA complex bound to AcrIIa2b at ~3.9 Å resolution (Figures 5A, 5B, and S1B). In the SpyCas9-sgRNA-AcrIIA2b complex, AcrIIA2b is positioned in the PAM duplex DNA binding cleft, between the NUC and REC lobes. It occupies the same position as that occupied by AcrIIA2 (Figure 5C), although AcrIIA2b buries a larger solvent-accessible surface area (~2,407 Å$^2$) upon ternary complex formation relative to AcrIIA2-Cas9 interface (~1,803 Å$^2$) (Figure S3D). Despite a large sequence disparity, AcrIIA2b shares the same fold ($\alpha1\alpha2\beta1\beta2\beta3\alpha3\beta4$) as AcrIIA2, and its overall structure is similar (Figures S4C and S4G). Divergent loop regions form the binding crevice (Figures S3F, S3G, and S4E). Additionally, the SpyCas9 conformation observed in the AcrIIA2b-bound structure is nearly identical to that observed in the AcrIIA2-bound structure (Figure 5C), except that the Hel-II domain within the REC lobe undergoes an intermediate conformational change (Figures S3E and S3F).

Although AcrIIA2b utilizes a nearly identical binding mode to that deployed by AcrIIA2 to inhibit SpyCas9 enzymatic activity (Figure 5D), a closer inspection of the AcrIIA2b binding crevice near the PAM-interacting site revealed a distinct local environment for interference with PAM recognition. Specifically, the two hydrophobic aromatic amino acid residues (Y39 and F94 in AcrIIA2b) that are engaged in hydrophilic and hydrophobic interactions with SpyCas9's PAM-interacting residues are either not present or not involved in interfering with PAM recognition by AcrIIA2 (Figure 5E). Interestingly, this interaction pattern of AcrIIA2b bears a striking resemblance to that of AcrIIA4 (Figure 5F), although the two anti-CRISPRs are evolutionarily unrelated. Additionally, the residues that AcrIIA2b and AcrIIA4 bind are evolutionarily conserved in Cas9 orthologs from across *Listeria* to closely related Cas9 orthologs from *Enterococcus* species (Figure 5G). Based on these structural observations, we deduced that the presence of aromatic hydrophobic residues in the PAM-interacting site may contribute to the prominent *in vitro* and *in vivo* inhibitory function exerted by both AcrIIA2b and AcrIIA4, and that loss of this extensive hydrophobic interaction pattern in the AcrIIA2-Cas9 interface makes it less stable and therefore less effective for inhibiting SpyCas9 function.

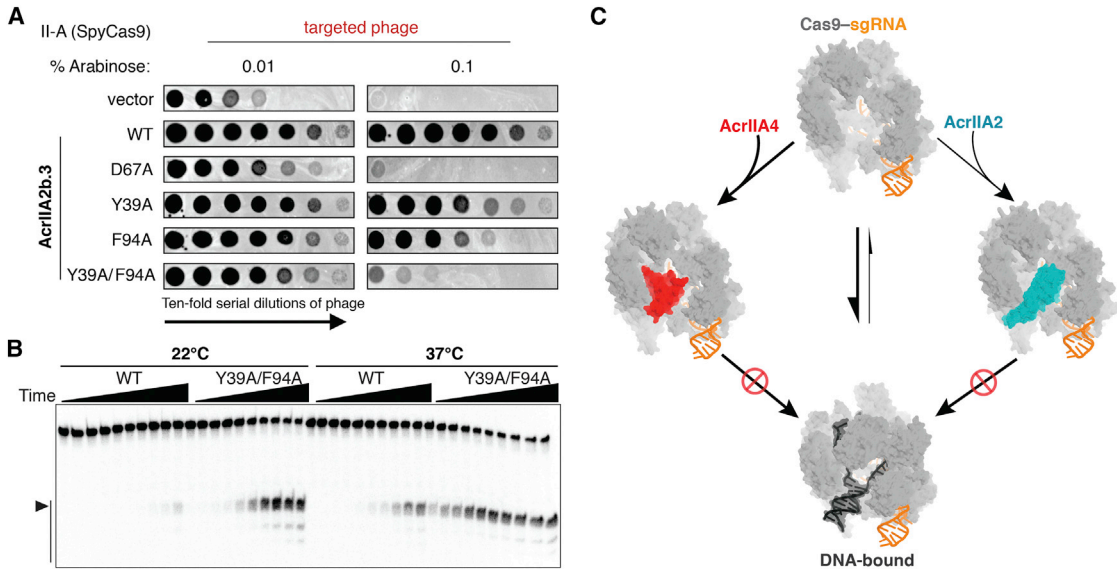


**Figure 6. A Convergent Cas9 Inhibition Mechanism Shared by AcrIIA2 and AcrIIA4**

(A) Plaquing of *P. aeruginosa* phage targeted by SpyCas9 in the presence of wild-type AcrIIA2b or the relevant point mutants. Double mutation of Y39A/F94A results in a large reduction of AcrIIA2b inhibition.

(B) *In vitro* cleavage assay showing the double mutation is more vulnerable and sensitive to temperature.

(C) Model of AcrIIA2 and AcrIIA4 convergent inhibition of SpyCas9's target DNA binding and cleavage activities.

To test this idea, we performed temperature- and urea-induced denaturation experiments on the SpyCas9-sgRNA-AcrIIA2b ternary complex and found that AcrIIA2b-SpyCas9 binding is more resistant to denaturation than is AcrIIA2a-SpyCas9 binding. To further assess the importance of individual residues for the inhibitory function of AcrIIA2b, we designed single and double amino acid substitutions and tested them using the *in vivo* anti-CRISPR activity assay in *P. aeruginosa* (Figure 4B). Substitution of Y39 or F94 for a small hydrophobic (Ala) residue had little impact on anti-CRISPR activity, whereas a Y39A/F94A double substitution and D67A mutation decreased activity significantly, when faced with high Cas9 levels (Figure 6A). *In vitro*, the Y39A/F94A double mutant showed a modest reduction in AcrIIA2b inhibition activity at low temperature but displayed a pronounced temperature-dependent anti-CRISPR activity, with the inhibition entirely ablated at body temperature (Figures 6B, S7B, and S7C). We concluded that the pattern of hydrophobic and hydrophilic residues surrounding the PAM-binding site is important to the function of anti-CRISPRs and that anti-CRISPR stability and efficiency can be altered by large hydrophobic aromatic amino acid residues.

## DISCUSSION

### A Convergent Cas9 Inhibition Mechanism Between AcrIIA2 and AcrIIA4

Bacteriophages have evolved anti-CRISPRs to counteract bacterial CRISPR-Cas adaptive immunity. Anti-CRISPRs have diverse sequences ranging from 50 to 150 amino acids that lack similarity to previously reported structures (Bondy-Denomy, 2018; Pawluk et al., 2018). AcrIIA2 and AcrIIA4 represent the first example of anti-CRISPR proteins that can circumvent CRISPR-Cas targeting mediated by both type II-A *L. monocytogenes and S. pyogenes* Cas9 enzymes. Although previous biochemical studies indicated AcrIIA2 blocks SpyCas9-DNA binding (Dong et al., 2017; Yang and Patel, 2017), it was unclear whether this inhibitor interferes with DNA binding directly or instead acts allosterically without directly competing with the DNA binding site. Here, we found that AcrIIA2 impedes PAM recognition and initial target DNA binding by directly occupying the PAM-interacting cleft on the sgRNA-loaded SpyCas9. In contrast to target DNA binding, which induces a large conformational change in the HNH and helical domains of SpyCas9, AcrIIA2 binding induces only a slight conformational change within SpyCas9.

Although AcrIIA2 and AcrIIA4 are unrelated anti-CRISPRs, their inhibition mechanisms both involve competitive inhibition of SpyCas9's PAM recognition (Figure 6C). In spite of the lack of global sequence and structural similarity, these two anti-CRISPRs make almost identical local contacts to inhibit Cas9 PAM recognition (Figures 5E and 5F). This commonality of the PAM-interference pocket but difference in Acr protein fold indicates that the PAM-interference capability evolved convergently in the AcrIIA2 and AcrIIA4 inhibitor families. Notably, previous phylogenetic analyses revealed that AcrIIA2 and AcrIIA4 are mutually exclusive in prophage genomes (Rauch et al., 2017). This suggests that despite often encoding multiple *acrIIA* genes, these phages and prophages do not co-encode anti-CRISPRs with redundant and competing binding sites. It is also worth noting that, although many characterized anti-CRISPRs prevent target DNA binding (Bondy-Denomy et al., 2015), AcrIIA2 and AcrIIA4 are the only two examples to date that function by specifically blocking PAM recognition.

### Temperature-Dependent Anti-CRISPR Activity and Implications for Genome Editing Control

*In vitro* assays revealed temperature-dependent anti-CRISPR inhibitory activity, with AcrIIA2 exhibiting a more pronounced temperature dependence compared to AcrIIA4. This observation may explain why AcrIIA2 can only partially inhibit SpyCas9 activity *in vivo*. The reduced temperature sensitivity of the AcrIIA2b homolog, which employs large aromatic residues to stabilize a favorable hydrophobic interaction on SpyCas9, also favors more robust Cas9 inhibition *in vivo*.

Previous studies have revealed that simultaneous delivery of AcrIIA4 with SpyCas9-sgRNA (RNP) complex inhibits Cas9-mediated gene targeting and that proper timing of AcrIIA4 delivery can reduce off-target editing while retaining on-target editing levels (Shin et al., 2017). We expect that AcrIIA2 can be employed in a similar manner to AcrIIA4 for regulating Cas9 *in vivo* genome editing. The reduced temperature sensitivity of AcrIIA2b relative to AcrIIA2a supports the use of AcrIIA2b for future applications due to more robust inhibitory activity. Our studies provide a basis for structure-based design of efficacious peptide modulators or even small molecular inhibitors that specifically interfere with PAM recognition. With more structures of anti-CRISPRs solved in the near future, we hope to better understand their diverse inhibitory mechanisms, enriching our current knowledge of how anti-CRISPRs are used to leverage the bacteria-phage arms race.

## STAR★METHODS

Detailed methods are provided in the online version of this paper and include the following:

- KEY RESOURCES TABLE
- CONTACT FOR REAGENT AND RESOURCE SHARING
- EXPERIMENTAL MODEL AND SUBJECT DETAILS
  - Microbes
- METHOD DETAILS
  - Bacterial Strains, Bacteriophages, and Plasmids
  - Construction of the Type II-A *Pseudomonas aeruginosa* Strain
  - Phage Plaquing Assays
  - Protein Expression and Purification
  - *In Vitro* Transcription and Purification of sgRNA
  - Reconstitution of the SpyCas9-sgRNA-AcrIIA2 Ternary Complex
  - Cryo-EM Microscopy
  - Images Processing and Reconstruction
  - Atomic Model Building and Validation
  - Analytical Size-Exclusion Chromatography Assay
  - *In Vitro* DNA Cleavage Assay
  - Competition Electrophoretic Mobility Shift Assays (EMSA)
  - Dissociation Kinetic EMSA
  - Urea Denaturation Assay
  - Heat Denaturation Assay
- DATA AND SOFTWARE AVAILABILITY
  - Data Resource

## SUPPLEMENTAL INFORMATION

Supplemental Information includes one table and seven figures and can be found online at https://doi.org/10.1016/j.molcel.2018.11.016.

## ACKNOWLEDGMENTS

This research was developed with funding from the Defense Advanced Research Projects Agency (DARPA) award HR0011-17-2-0043. The views, opinions, and/or findings expressed are those of the author and should not be interpreted as representing the official views or policies of the Department of Defense or the U.S. government. Approved for public release; distribution is unlimited. The cryo-EM data were collected in the EM facility of University of California, Berkeley. We are thankful to D. Toso and P. Grob for expert electron microscopy assistance and A. Chintangal and P. Tobias for computational support. We also thank members of the Bondy-Denomy, Doudna, and Nogales labs for helpful discussions. F.J. is a Merck Fellow of the Damon Runyon Cancer Research (DRG-2201-14). J.B.-D. is supported by the University of California San Francisco Program for Breakthrough in Biomedical Research, funded in part by the Sandler Foundation, and an NIH Office of the Director Early Independence Award (DP5-OD021344). J.A.D. and E.N. are Investigators of the Howard Hughes Medical Institute.

## AUTHOR CONTRIBUTIONS

F.J., J.B.-D., and J.A.D. designed experiments; F.J. and M.X. performed biochemistry experiments; F.J. and J.-J.L. performed structural studies; B.A.O. and J.D.B. prepared strains; B.A.O. conducted mutagenesis and executed phage-plaquing experiments; B.J.R. and J.B.-D. conducted bioinformatics analysis of AcrIIA2 proteins; J.A.D., J.B.-D., and E.N. supervised experiments; F.J., J.B.-D., and J.A.D. wrote the manuscript with input from all authors.

## DECLARATION OF INTERESTS

A patent has been filed pertaining to AcrIIA genes and their applications. J.A.D. is a co-founder of Caribou Biosciences, Editas Medicine, Intellia Therapeutics, Scribe Therapeutics, and Mammoth Biosciences. J.A.D. is a scientific advisory board member of Caribou Biosciences, Intellia Therapeutics, eFFECTOR Therapeutics, Scribe Therapeutics, Synthego, Metagenomi, Mammoth Biosciences, and Inari. J.A.D. is a member of the board of directors at Driver and Johnson & Johnson and has sponsored research projects by Pfizer, Roche Biopharma, and Biogen. J.B.-D. is a scientific advisory board member of SNIPR Biome and Excision Biotherapeutics.

Received: September 4, 2018
Revised: October 23, 2018
Accepted: November 14, 2018
Published: December 27, 2018

## REFERENCES

Adams, P.D., Afonine, P.V., Bunkóczi, G., Chen, V.B., Davis, I.W., Echols, N., Headd, J.J., Hung, L.-W., Kapral, G.J., Grosse-Kunstleve, R.W., et al. (2010). PHENIX: a comprehensive Python-based system for macromolecular structure solution. Acta Crystallogr. D Biol. Crystallogr. *66*, 213–221.

Afonine, P.V., Poon, B.K., Read, R.J., Sobolev, O.V., Terwilliger, T.C., Urzhumtsev, A., and Adams, P.D. (2018). Real-space refinement in PHENIX for cryo-EM and crystallography. Acta Crystallogr D Struct Biol *74*, 531–544.

Anders, C., Niewoehner, O., Duerst, A., and Jinek, M. (2014). Structural basis of PAM-dependent target DNA recognition by the Cas9 endonuclease. Nature *513*, 569–573.

Barrangou, R., and Marraffini, L.A. (2014). CRISPR-Cas systems: prokaryotes upgrade to adaptive immunity. Mol. Cell *54*, 234–244.

Basgall, E.M., Goetting, S.C., Goeckel, M.E., Giersch, R.M., Roggenkamp, E., Schrock, M.N., Halloran, M., and Finnigan, G.C. (2018). Gene drive inhibition

by the anti-CRISPR proteins AcrIIA2 and AcrIIA4 in Saccharomyces cerevisiae. Microbiology *164*, 464–474.

Bondy-Denomy, J., Pawluk, A., Maxwell, K.L., and Davidson, A.R. (2013). Bacteriophage genes that inactivate the CRISPR/Cas bacterial immune system. Nature *493*, 429–432.

Bondy-Denomy, J. (2018). Protein inhibitors of CRISPR-Cas9. ACS Chem. Biol. *13*, 417–423.

Bondy-Denomy, J., Garcia, B., Strum, S., Du, M., Rollins, M.F., Hidalgo-Reyes, Y., Wiedenheft, B., Maxwell, K.L., and Davidson, A.R. (2015). Multiple mechanisms for CRISPR-Cas inhibition by anti-CRISPR proteins. Nature *526*, 136–139.

Borges, A.L., Davidson, A.R., and Bondy-Denomy, J. (2017). The discovery, mechanisms, and evolutionary impact of anti-CRISPRs. Annu Rev Virol *4*, 37–59.

Chen, V.B., Arendall, W.B., 3rd, Headd, J.J., Keedy, D.A., Immormino, R.M., Kapral, G.J., Murray, L.W., Richardson, J.S., and Richardson, D.C. (2010). MolProbity: all-atom structure validation for macromolecular crystallography. Acta Crystallogr. D Biol. Crystallogr. *66*, 12–21.

Choi, K.-H., and Schweizer, H.P. (2006). mini-Tn7 insertion in bacteria with single attTn7 sites: example Pseudomonas aeruginosa. Nat. Protoc. *1*, 153–161.

Dong, D., Guo, M., Wang, S., Zhu, Y., Wang, S., Xiong, Z., Yang, J., Xu, Z., and Huang, Z. (2017). Structural basis of CRISPR-SpyCas9 inhibition by an anti-CRISPR protein. Nature *546*, 436–439.

Emsley, P., and Cowtan, K. (2004). Coot: model-building tools for molecular graphics. Acta Crystallogr. D Biol. Crystallogr. *60*, 2126–2132.

Grant, G.A. (2006). The ACT domain: a small molecule binding domain and its role as a common regulatory element. J. Biol. Chem. *281*, 33825–33829.

Hale, C.R., Zhao, P., Olson, S., Duff, M.O., Graveley, B.R., Wells, L., Terns, R.M., and Terns, M.P. (2009). RNA-guided RNA cleavage by a CRISPR RNA-Cas protein complex. Cell *139*, 945–956.

Hille, F., and Charpentier, E. (2016). CRISPR-Cas: biology, mechanisms and relevance. Philos. Trans. R. Soc. Lond. B Biol. Sci. *371*, 20150496.

Hynes, A.P., Rousseau, G.M., Lemay, M.-L., Horvath, P., Romero, D.A., Fremaux, C., and Moineau, S. (2017). An anti-CRISPR from a virulent streptococcal phage inhibits Streptococcus pyogenes Cas9. Nat. Microbiol. *2*, 1374–1380.

Hynes, A.P., Rousseau, G.M., Agudelo, D., Goulet, A., Amigues, B., Loehr, J., Romero, D.A., Fremaux, C., Horvath, P., Doyon, Y., et al. (2018). Widespread anti-CRISPR proteins in virulent bacteriophages inhibit a range of Cas9 proteins. Nat. Commun. *9*, 2919.

Jiang, F., Zhou, K., Ma, L., Gressel, S., and Doudna, J.A. (2015). STRUCTURAL BIOLOGY. A Cas9-guide RNA complex preorganized for target DNA recognition. Science *348*, 1477–1481.

Jiang, F., Taylor, D.W., Chen, J.S., Kornfeld, J.E., Zhou, K., Thompson, A.J., Nogales, E., and Doudna, J.A. (2016). Structures of a CRISPR-Cas9 R-loop complex primed for DNA cleavage. Science *351*, 867–871.

Kimanius, D., Forsberg, B.O., Scheres, S.H., and Lindahl, E. (2016). Accelerated cryo-EM structure determination with parallelisation using GPUs in RELION-2. eLife *5*, e18722.

Koonin, E.V., Makarova, K.S., and Zhang, F. (2017). Diversity, classification and evolution of CRISPR-Cas systems. Curr. Opin. Microbiol. *37*, 67–78.

Li, C., Psatha, N., Gil, S., Wang, H., Papayannopoulou, T., and Lieber, A. (2018). HDAd5/35$^{++}$ adenovirus vector expressing anti-CRISPR peptides decreases CRISPR/Cas9 toxicity in human hematopoietic stem cells. Mol. Ther. Methods Clin. Dev. *9*, 390–401.

Liu, X.S., Wu, H., Krzisch, M., Wu, X., Graef, J., Muffat, J., Hnisz, D., Li, C.H., Yuan, B., Xu, C., et al. (2018). Rescue of fragile X syndrome neurons by DNA methylation editing of the FMR1 Gene. Cell *172*, 979–992.e6.

Makarova, K.S., Wolf, Y.I., Alkhnbashi, O.S., Costa, F., Shah, S.A., Saunders, S.J., Barrangou, R., Brouns, S.J.J., Charpentier, E., Haft, D.H., et al. (2015). An updated evolutionary classification of CRISPR-Cas systems. Nat. Rev. Microbiol. *13*, 722–736.

Marraffini, L.A. (2015). CRISPR-Cas immunity in prokaryotes. Nature *526*, 55–61.

Marraffini, L.A., and Sontheimer, E.J. (2008). CRISPR interference limits horizontal gene transfer in staphylococci by targeting DNA. Science *322*, 1843–1845.

Marraffini, L.A., and Sontheimer, E.J. (2010). CRISPR interference: RNA-directed adaptive immunity in bacteria and archaea. Nat. Rev. Genet. *11*, 181–190.

Mindell, J.A., and Grigorieff, N. (2003). Accurate determination of local defocus and specimen tilt in electron microscopy. J. Struct. Biol. *142*, 334–347.

Nishimasu, H., Ran, F.A., Hsu, P.D., Konermann, S., Shehata, S.I., Dohmae, N., Ishitani, R., Zhang, F., and Nureki, O. (2014). Crystal structure of Cas9 in complex with guide RNA and target DNA. Cell *156*, 935–949.

Pawluk, A., Amrani, N., Zhang, Y., Garcia, B., Hidalgo-Reyes, Y., Lee, J., Edraki, A., Shah, M., Sontheimer, E.J., Maxwell, K.L., et al. (2016). Naturally occurring off-switches for CRISPR-Cas9. Cell *167*, 1829–1838.

Pawluk, A., Davidson, A.R., and Maxwell, K.L. (2018). Anti-CRISPR: discovery, mechanism and function. Nat. Rev. Microbiol. *16*, 12–17.

Punjani, A., Rubinstein, J.L., Fleet, D.J., and Brubaker, M.A. (2017). cryoSPARC: algorithms for rapid unsupervised cryo-EM structure determination. Nat. Methods *14*, 290–296.

Rauch, B.J., Silvis, M.R., Hultquist, J.F., Waters, C.S., McGregor, M.J., Krogan, N.J., and Bondy-Denomy, J. (2017). Inhibition of CRISPR-Cas9 with bacteriophage proteins. Cell *168*, 150–158.e10.

Rohou, A., and Grigorieff, N. (2015). CTFFIND4: Fast and accurate defocus estimation from electron micrographs. J. Struct. Biol. *192*, 216–221.

Shin, J., Jiang, F., Liu, J.-J., Bray, N.L., Rauch, B.J., Baik, S.H., Nogales, E., Bondy-Denomy, J., Corn, J.E., and Doudna, J.A. (2017). Disabling Cas9 by an anti-CRISPR DNA mimic. Sci. Adv. *3*, e1701620.

Sontheimer, E.J., and Davidson, A.R. (2017). Inhibition of CRISPR-Cas systems by mobile genetic elements. Curr. Opin. Microbiol. *37*, 120–127.

Sternberg, S.H., Redding, S., Jinek, M., Greene, E.C., and Doudna, J.A. (2014). DNA interrogation by the CRISPR RNA-guided endonuclease Cas9. Nature *507*, 62–67.

Tang, G., Peng, L., Baldwin, P.R., Mann, D.S., Jiang, W., Rees, I., and Ludtke, S.J. (2007). EMAN2: an extensible image processing suite for electron microscopy. J. Struct. Biol. *157*, 38–46.

van Heel, M., Harauz, G., Orlova, E.V., Schmidt, R., and Schatz, M. (1996). A new generation of the IMAGIC image processing system. J. Struct. Biol. *116*, 17–24.

Wiedenheft, B., van Duijn, E., Bultema, J.B., Waghmare, S.P., Zhou, K., Barendregt, A., Westphal, W., Heck, A.J., Boekema, E.J., Dickman, M.J., and Doudna, J.A. (2011). RNA-guided complex from a bacterial immune system enhances target recognition through seed sequence interactions. Proc. Natl. Acad. Sci. USA *108*, 10092–10097.

Yang, H., and Patel, D.J. (2017). Inhibition mechanism of an anti-CRISPR suppressor AcrIIA4 targeting SpyCas9. Mol. Cell *67*, 117–127.e5.

Zheng, S.Q., Palovcak, E., Armache, J.-P., Verba, K.A., Cheng, Y., and Agard, D.A. (2017). MotionCor2: anisotropic correction of beam-induced motion for improved cryo-electron microscopy. Nat. Methods *14*, 331–332.

## STAR★METHODS

### KEY RESOURCES TABLE

| REAGENT or RESOURCE | SOURCE | IDENTIFIER |
|---|---|---|
| Bacterial and Virus Strains | | |
| *Pseudomonas aeruginosa* | This paper | see Figure 4 |
| *P. aeruginosa* phage, JBD30 | This paper | see Figure 4 |
| *Escherichia coli* BL21 Star (DE3) | ThermoFisher | N/A |
| *Escherichia coli* DH5 alpha | ThermoFisher | N/A |
| Chemicals, Peptides, and Recombinant Proteins | | |
| T7 RNA polymerase | Homemade | N/A |
| PreScission protease | Homemade | N/A |
| Ulp1 protease | ThermoFisher | Cat#12588018 |
| T4 polynucleotide kinase | NEB | Cat#M0201S |
| Urea | Sigma-Aldrich | Cat#U5378-5KG |
| 40% acrylamide and bis-acrylamide solution, 29:1 | Fisher Scientific | Cat#BP1408-1 |
| Critical Commercial Assays | | |
| In-Fusion HD Cloning Kit | Clontech | Cat#638920 |
| Plasmid Megaprep Kit | QIAGEN | Cat#12183 |
| Gibson Assembly Cloning Kit | NEB | Cat#E2611 |
| Deposited Data | | |
| Cryo-EM map of SpyCas9-sgRNA-AcrIIA2 complex | This paper | EMDB: 9066 |
| Coordinate of SpyCas9-sgRNA-AcrIIA2 complex | This paper | PDB: 6MCB |
| Cryo-EM map of SpyCas9-sgRNA-AcrIIA2b complex | This paper | EMDB: 9067 |
| Coordinate of SpyCas9-sgRNA-AcrIIA2b complex | This paper | PDB: 6MCC |
| Oligonucleotides | | |
| Non-target DNA strand: GCAACTACGGCGCATAAAGATGAGACGCGGG CGATTAGTACACGCAAAAG | This paper | N/A |
| Target DNA strand: CTTTTGCGTGTACTAATCGCCCGCGTCTCATCTTT ATGCGCCGTAGTTGC | This paper | N/A |
| Recombinant DNA | | |
| $P_{BAD}$-SpyCas9 | This paper | N/A |
| $P_{BAD}$-sgRNA | This paper | N/A |
| A modified pET28b-His-SUMO-AcrIIA2 | This paper | N/A |
| pGEX-6P-1-GST-AcrIIA2b | This paper | N/A |
| Software and Algorithms | | |
| Motioncor2 | Zheng et al., 2017 | http://msg.ucsf.edu/em/software/motioncor2.html |
| CTFFIND4 | Rohou and Grigorieff, 2015 | http://grigoriefflab.janelia.org/ctffind4 |
| EMAN2 | Tang et al., 2007 | https://blake.bcm.edu/emanwiki/EMAN2 |
| IMAGIC | van Heel et al., 1996 | https://www.imagescience.de/imagic.html |
| Gautomatch | written by Dr. Kai Zhang | https://www.mrc-lmb.cam.ac.uk/kzhang/ |
| CryoSPARC | Punjani et al., 2017 | https://cryosparc.com |
| RELION-2.0 | Kimanius et al., 2016 | https://www2.mrc-lmb.cam.ac.uk/relion/ |
| Coot | Emsley and Cowtan, 2004 | https://www2.mrc-lmb.cam.ac.uk/personal/pemsley/coot/ |

(*Continued on next page*)

*Continued*

| REAGENT or RESOURCE | SOURCE | IDENTIFIER |
|---|---|---|
| PHENIX | Afonine et al., 2018 | https://www.phenix-online.org |
| Chimera | UCSF | https://www.cgl.ucsf.edu/chimera/ |
| PyMOL | Schrodinger LLC | https://pymol.org |
| Prism6.0 | GraphPad Software | https://www.graphpad.com/scientific-software/prism/ |

## CONTACT FOR REAGENT AND RESOURCE SHARING

Further information and requests for reagents could be directed to and will be fulfilled by Jennifer A. Doudna (doudna@berkeley.edu).

## EXPERIMENTAL MODEL AND SUBJECT DETAILS

### Microbes

Plasmid DNA for *in vitro* transcription was amplified in *Escherichia coli* DH5α strain in Lysogeny broth (LB) medium at 37°C overnight. Recombinant proteins were overexpressed in *E. coli* BL21 Star (DE3) strain in Terrific Broth (TB) medium. The cells were grown at 37°C until $OD_{600}$ reached 0.6∼0.8 and then induced with 0.20 mM Isopropyl b-D-1-thiogalactopyranoside (IPTG) at 18°C for 16 hr. *Pseudomonas* aeruginosa (PAO1) were cultured on LB agar or liquid media at 37°C. *P. aeruginosa* DMS3m-like phages (JBD30 and its derivative JBD30-IIA-escaper) were amplified on PAO1 and stored in SM buffer at 4°C.

## METHOD DETAILS

### Bacterial Strains, Bacteriophages, and Plasmids

*P.* aeruginosa (PAO1) and *E. coli* (DH5a, for plasmid maintenance) were cultured on LB agar or liquid media at 37°C. LB was supplemented with gentamicin (50 μg/mL for *P. aeruginosa*, 30 μg/mL for *E. coli*) to maintain the pHERD30T plasmid or carbenicillin (250 μg/mL for *P. aeruginosa*, 100 μg/mL for *E. coli*) to maintain pMMB67HE. To maintain pHERD30T and pMMB67HE in the same strain of *P. aeruginosa*, double selection of 30 μg/mL gentamicin and 100 μg/mL carbenicillin was employed. In all *P. aeruginosa* experiments, expression from pHERD30T was induced with 0.001%, 0.01%, or 0.1% arabinose and expression from pMMB67HE was induced with 0.5mM Isopropyl b-D-1-thiogalactopyranoside (IPTG). *Pseudomonas aeruginosa* DMS3m-like phages (JBD30 and its derivative JBD30-IIA-escaper) were amplified on PAO1 and stored in SM buffer at 4°C. All anti-CRISPR genes were introduced into the pMMB67HE vector by Gibson assembly.

### Construction of the Type II-A *Pseudomonas aeruginosa* Strain

SpyCas9 expressed from the $P_{BAD}$ promoter of a modified pUC18T-mini-Tn7T-Gm plasmid (a gift from Jason Peters in the Carol Gross lab) was integrated into the *P. aeruginosa* strain PAO1 chromosome by electroporation and Flp-mediated marker excision as previously described (Choi and Schweizer, 2006). The resulting PAO1-attTn7::pUC18T-miniTn7T-$P_{BAD}$-SpyCas9 strain was transformed with pJBD428 (p30T-$P_{BAD}$-sgRNA) by electroporation, generating the heterologous Type II-A PAO1 strain bJBD311.

### Phage Plaquing Assays

A bacterial lawn was generated by spreading 3 mL of top agar seeded with 150 mL of host bacteria on a LB agar plate supplemented with 10 mM $MgSO_4$, 30 μg/mL gentamicin, 200 μg/mL carbenicillin, 0.001%, 0.01%, or 0.1% arabinose, and 0.5mM IPTG. 3 μL of phage serially diluted in SM buffer was then spotted onto the lawn and incubated at 30°C for 16 hr. Plate images were collected using the Gel Doc EZ Gel Documentation System (Bio-Rad) and Image Lab (Bio-Rad) software.

### Protein Expression and Purification

Recombinant wild-type *Streptococcus pyogenes* Cas9 (SpyCas9) was expressed in *Escherichia coli* strain BL21 Star (DE3) (Thermo Fisher Scientific) and purified to homogeneity as described previously (Jiang et al., 2015). The genes encoding full-length *acrIIA2* and *acrIIA4* were subcloned into a modified pET28b expression vector with a N-terminal His6-SUMO fusion tag and a Ulp1 protease site at the N terminus. The phage-encoded anti-CRISPR *acrIIA2* homologous gene (*acrIIA2b.3* or *acrIIA2b*) was inserted into a pGEX-6P-1 expression vector (GE Healthcare) with a N-terminal GST affinity tag and a PreScission protease site. All the anti-CRISPR proteins mentioned above were overexpressed in *E. coli* BL21 Star (DE3) strain and affinity purified using nickel-nitrilotriacetic acid (Ni-NTA) agarose resin (QIAGEN) with the elution buffer (25 mM Tris-HCl pH 8.0, 300 mM NaCl, 5% glycerol, and 150 mM imidazole). After removing the respective affinity tag by appropriate protease through overnight proteolysis at 4°C in 20 mM HEPES pH 7.0, 100 mM NaCl, 5 mM DTT and 5% glycerol, the fractions containing the recombinant proteins were loaded onto the prepacked HiTrap Q Fast Flow column (GE Healthcare). The tag-free anti-CRPSR proteins were then eluted with a linear NaCl gradient of 100–1000 mM, followed by gel filtration chromatography (HiLoad 16/60 Superdex75, GE Healthcare) in 30 mM HEPES pH 7.5, 150 mM NaCl, 5 mM

DTT, and 10% glycerol. The relevant fractions were concentrated and flash-frozen in liquid nitrogen and stored in −80°C. The mutants, including (Y39A/F94A) of AcrIIA2b.3, were constructed using site-directed mutagenesis with Clontech's In-Fusion cloning system and purified by the same method as described above.

### *In Vitro* Transcription and Purification of sgRNA

The sgRNA was transcribed *in vitro* using a linearized plasmid DNA as the template. Large-scale transcription reactions (10 mL) were carried out in buffer containing 50 mM Tris-HCl pH 8.0, 10 mM DTT, 50 mM $MgCl_2$, 0.1% Triton X-100, 2 mM spermidine, 4 mM each NTP, 1 mg home-made T7 RNA polymerase, 0.5 mg DNA template, and RNase Inhibitor (Promega). The mixture was incubated at 37°C for 4 hr and the reaction was stopped by ethanol precipitation. The re-dissolved RNA was purified by 10% denaturing TBE-urea PAGE, with the excised band containing sgRNA passively eluted into DEPC-treated water overnight at 4°C. The eluted RNA was then concentrated and buffer exchanged into RNase-free water by ultrafiltration (Millipore). The final purified sgRNA was denatured at 95°C for 5 min followed by slowly cooling to room temperature before freezing in −20°C.

The sgRNA sequence for *in vitro* transcription (from 5′ to 3′):

GGCGCAUAAAGAUGAGACGCGUUUUAGAGCUAUGCUGUUUUGAAAAAAACAGCAUAGCAAGUUAAAAUAAGGCUAGUCCGUUAUCAACUUGAAAAAGUGGCACCGAGUCGGUGCUU

### Reconstitution of the SpyCas9-sgRNA-AcrIIA2 Ternary Complex

Reconstitution of the Cas9-sgRNA-AcrIIA2 complex was carried out by mixing purified SpyCas9 and *in vitro* transcribed sgRNA in a 1:1.5 molar ratio at room temperature for 15 min before adding three molar excess of AcrIIA2. The reconstituted ternary complex was further purified by analytical size-exclusion chromatography (Superdex 200 Increase 10/300 GL column, GE Healthcare) pre-equilibrated with the buffer containing 30 mM Tris-HCl pH 8.0, 150 mM NaCl, 5 mM DTT. The eluted ternary complex was analyzed by SDS-PAGE and the relevant fractions containing both AcrIIA2 and SpyCas9 were further concentrated by a spin concentrator (10-kDa cutoff) prior to biochemical and structural studies. The concentration of the Cas9-sgRNA-AcrIIA2 ternary complex was estimated by UV absorption, with the sum of SpyCas9, AcrIIA2, and sgRNA extinction coefficients at 260 nm.

### Cryo-EM Microscopy

SpyCas9-sgRNA-AcrIIA2 complexes in a buffer containing 30 mM Tris-HCl (pH8.0), 150 mM NaCl, 5mM DTT and 0.1% glycerol were used for cryo-EM sample preparation. Immediately after glow-discharging the grid for 14 s using a Solaris plasma cleaner, 3.7 μL droplets of the sample (~3 μM) were placed onto C-flat grids with 2 μm holes and 2 μm spacing between holes (Protochips). The grids were rapidly plunged into liquid ethane using an FEI Vitrobot MarkIV maintained at 8°C and 100% humidity, after being blotted for 4.5 s with a blot force of 10. Data were acquired using an FEI Titan Krios transmission electron microscope (UC Berkeley) operated at 300 keV, at a nominal magnification of X 29,000 (0.83 Å pixel size), and with defocus ranging from −0.5 to −2.5 μm. A total of ~2,435 micrographs were recorded using SerialEM on a Gatan K2 Summit direct electron detector operated in counting mode. We collected a 7.25 s exposure fractionated into 29 frames (250 ms per frame) with a frame dose of 1.49 $e^-$ $Å^{-2}$.

SpyCas9-sgRNA-AcrIIA2b complexes in a buffer containing 30mM Tris-HCl (pH 8.0), 150mM NaCl, 5mM DTT and 0.1% glycerol were used for cryo-EM sample preparation. Immediately after glow-discharging the grid for 14 s using a Solaris plasma cleaner, 3.7 μL droplets of the sample (~2.5 μM) were placed onto C-flat grids with 2 μm holes and 2 μm spacing between holes (Protochips). The grids were rapidly plunged into liquid ethane using an FEI Vitrobot MarkIV maintained at 8°C and 100% humidity, after being blotted for 4.5 s with a blot force of 10. Data were acquired using an FEI Titan Krios transmission electron microscope (UC Berkeley) operated at 300 keV with energy filter, at a nominal magnification of × 105,000 (1.15 Å pixel size), and with defocus ranging from −0.7 to −2.7 μm. A total of ~2,868 micrographs were recorded using SerialEM on a Gatan K2 Summit direct electron detector operated in counting mode. We collected a 7.5 s exposure fractionated into 30, 250 ms frames with a frame dose of 1.54 $e^-$ $Å^{-2}$.

### Images Processing and Reconstruction

For SpyCas9-sgRNA-AcrIIA2 complexes, the 24 frames (we skipped the first 2 frames and last 3 frames) of each video in a super-resolution model were aligned, decimated, and summed and dose-weighted using Motioncor2 (Zheng et al., 2017). CTF values of the summed-micrographs were determined using CTFFIND4 (Mindell and Grigorieff, 2003) and then applied to dose-weighted summed-micrographs for further processing. Initial particle picking to generate template images was performed in EMAN2 (Tang et al., 2007). About 5,000 particles were selected and then imported into IMAGIC for reference-free 2D classification (van Heel et al., 1996). Particle picking for the complete dataset was carried out by using Gautomatch (https://www.mrc-lmb.cam.ac.uk/kzhang/) with templates generated in previous 2D classification. 870,002 were selected in total. All the particles were imported into CryoSPARC and 3D classified into 6 classes via *ab initio* modeling function (Punjani et al., 2017). Particles in the best class with intact Cas9 RNP architecture were further selected and 3D classified into 4 classes in CryoSPARC. Particles belong to the best class were further selected for homogeneous refinement. Local resolution was calculated with the half maps in RELION-2.0 (Kimanius et al., 2016). To avoid the loss of particles in rare orientations, 2D classification was skipped during the imaging processing of the whole dataset.

For SpyCas9-sgRNA-AcrIIA2b complexes, the 23 frames (we skipped the first 2 frames and last 5 frames) of each video in super-resolution model were aligned, decimated, and summed and dose-weighted using Motioncor2 (Zheng et al., 2017). CTF values of the summed-micrographs were determined by CTFFIND4 and then applied to dose-weighted summed-micrographs for further

processing (Rohou and Grigorieff, 2015). Particle picking was carried out by using Gautomatch with 2D templates generated in SpyCas9-sgRNA-AcrIIA2 dataset. 630107 particles were picked in total. For the stacked particles, we used the same 3D processing procedure as SpyCas9-sgRNA-AcrIIA2 dataset in CryoSPARC.

### Atomic Model Building and Validation

All atomic models were built using the crystal structure of SpyCas9sgRNA (PDB ID 4ZT0) as a template for CRISPR-Cas9 complex. The initial template was aligned with individual EM reconstructions with "Fit in Map" function of Chimera (UCSF). The aligned SpyCas9-sgRNA were then subjected to one cycle of rigid body fit, simulated annealing and/or morphing in PHENIX (Adams et al., 2010) before manual rebuilding in Coot (Emsley and Cowtan, 2004) to fit the EM density. To build the respective AcrIIA2 and AcrIIA2b atomic model into the attributable EM density aside from that corresponding to CRISPR-Cas9 complex, the secondary structure prediction and several amino acids with large side chains within anti-CRISPR proteins were used for registering the sequence length and *ab initio* model building in Coot. The full atomic model of SpyCas9-sgRNA-AcrIIA2 and SpyCas9-sgRNA-AcrIIA2b complexes were then subjected to the multiple rounds real space refinement in PHENIX (global minimization, atomic displacement parameter (ADP) refinement, local grid searches and secondary structure restraints, but no morphing, no simulated annealing in the last few rounds) with Ramachandran and nucleic acid restraints (Afonine et al., 2018). The final models were validated by RCSB PDB validation server and MolProbity (Chen et al., 2010). All statistics of the data processing and structure refinement of SpyCas9-sgRNA-AcrIIA2 and SpyCas9-sgRNA-AcrIIA2b complexes were summarized in Table S1. Structural analysis was conducted in Coot and figures were prepared using PyMOL (Schrodinger LLC) and UCSF Chimera. Model PDB file was converted into model density map and further aligned with the real EM map by EMAN2 (Tang et al., 2007). Model against Map FSC was then calculated between the aligned model density map and real EM map.

### Analytical Size-Exclusion Chromatography Assay

Analytical size-exclusion chromatography was conducted on an AKTA Purifier system (GE Healthcare). The wild-type SpyCas9 apoprotein was used in this assay alongside with 10 mM EDTA to prevent DNA cleavage activity. For the SpyCas9-sgRNA binary complex, SpyCas9 was incubated with sgRNAs at the molar ratio of 1:1.6 at room temperature for 30 min before applied onto the column. For the SpyCas9-sgRNA-dsDNA ternary complex, SpyCas9, sgRNA, and dsDNA were mixed at the molar ratio of 1:1.6:3 at room temperature for 30 min before loading onto the column. For the assays of the apo-SpyCas9 and AcrIIA (abbreviation for AcrIIA4, AcrIIA2 and its homolog AcrIIA2b), SpyCas9 and AcrIIA were mixed at the molar ratio of 1:3 and incubated at room temperature for 30 min. For the assays of the AcrIIA-bound sgRNA-SpyCas9, the purified SpyCas9 and sgRNA were mixed first at the molar ratio of 1:1.6 before adding AcrIIA at the molar ratio of 1:1.6:3 and incubated on the bench for 30 min. For the competition assay, the ternary complex samples were first purified by gel filtration and the pure ternary complexes were then mixed with appropriate competitors at the molar ratio of 1:5 and further incubated on ice overnight before loading onto the gel filtration column. Each sample was assayed on a Superdex 200 Increase 10/300 GL column (GE Healthcare) that was pre-equilibrated with a buffer containing 30 mM Tris-HCl pH 8.0, 150 mM NaCl, 10 mM EDTA, and 5 mM DTT. The relevant fractions are detected by 4%–20% SDS-PAGE. Eluates were simultaneously monitored by ultraviolet absorbance at 260 nm and 280 nm, respectively. For clarity, only spectra at 280 nm were shown in figures. Notably, the target and non-target DNA strands used in this study were purchased from IDT (Integrated DNA Technologies) and dissolved in DEPC-treated water. The target and non-target DNA strands were mixed together with a molar ratio of 1:1, and further annealed by heating up at 95°C for 5 min followed by slowly cooling to room temperature.

### *In Vitro* DNA Cleavage Assay

DNA Cleavage assays were run to quantify the ability of AcrII proteins to inhibit SpyCas9. Two single-stranded oligonucleotides containing 20-bp λ1 DNA target sequences and 5′-GGG-3′ PAM motifs were annealed to construct double-stranded DNA target (5′-GCAACTACGGCGCATAAAGATGAGACGC**GGG**CGATTAGTACACGCAAAAG-3′ and its complement). The DNA was 5′ end-labeled using [$\gamma$-$^{32}$P]-adenosine triphosphate (PerkinElmer) and T4 polynucleotide kinase (New England Biolabs). Unincorporated nucleotides were removed by spin-column chromatography using GE MicroSpin G-25 columns. Before cleavage reactions, SpyCas9 (final concentration 10 nM) and sgRNA (final concentration 100 nM) were pre-incubated in 5X cleavage buffer (50 mM HEPES pH 7.5, 500 mM NaCl, 5 mM DTT, 25 mM $MgCl_2$) at 22°C for 15 min. AcrII proteins (various concentrations) were added to the reaction mixtures and allowed to form SpyCas9-sgRNA-AcrII complexes at 22°C for 30 min. Approximate 10 fmol of radiolabeled DNA was added to each reaction mixture and incubated at 22°C or 37°C for various time points. The reactions were quenched by adding 2X RNA Loading Dye (95% formamide, 0.02% SDS, 0.02% bromophenol blue, 0.01% xylene cyanol, 25 mM EDTA). The cleaved DNA products were then run on 10% urea-denaturing polyacrylamide gels, which were pre-run for 30 min at 45 W before loading of samples and afterward run for 60 min at 45 W to resolve the cleavage products. The gels were dried and then visualized by phosphorimaging. Band intensity was further quantified using ImageQuant TL software (GE Healthcare) and fit to a binding isotherm using Prism (GraphPad Software).

### Competition Electrophoretic Mobility Shift Assays (EMSA)

EMSA assays were run to measure the kinetic competition between DNA and AcrII proteins as AcrII concentration increases. The DNA substrate was the same as that used for the SpyCas9 cleavage assays. Before addition of radiolabeled DNA, SpyCas9-sgRNA

complex (final concentration 100 nM) was purified and diluted in 5X protein binding buffer (1 mg/mL tRNA, 0.25% NP-40, 500 mM NaCl, 25 mM EDTA, 50 mM HEPES pH 7.5, 10% glycerol). Notably, 5 mM ethylenediaminetetraacetic acid (EDTA) was included to prevent any potential DNA cleavage. Approximate 10 fmol of radiolabeled DNA was added to the reaction mixtures and allowed to form SpyCas9-sgRNA-dsDNA complexes at 22°C for 30 min. AcrII proteins with various concentrations were then added to the reaction mixtures and allowed to incubate at 22°C for 30 min. In a parallel experiment, radiolabeled DNA probe were mixed with AcrIIA before adding to SpyCas9-sgRNA complex. All the reactions were equilibrated for 30 min at room temperature before mixed with 2X native loading buffer (62.5 mM Tris-HCl pH 6.8, 40% glycerol, 0.01% bromophenol blue). The samples were resolved on 8% native polyacrylamide gels which were pre-run at 10 W for 30 min before loading of samples; afterward, the gels were run at 20 W for 90 min to resolve the DNA-bound complexes and free DNA. The gels were dried, visualized by phosphorimaging, and quantified using GE ImageQuant TL.

### Dissociation Kinetic EMSA

EMSA were also run to measure the dissociation of DNA due to AcrII proteins over long time-courses. The DNA substrate was the same as that used for SpyCas9 cleavage assays. Before addition of radiolabeled DNA, SpyCas9-sgRNA complex (final concentration 100 nM) was purified and diluted in 5X protein binding buffer. Approximate 10 fmol of radiolabeled DNA was added to the reaction mixtures and allowed to form SpyCas9-sgRNA-dsDNA complexes at 22°C for 30 min. AcrII proteins (final concentration 500 nM) were then added to respective reaction mixtures and allowed to incubate at 22°C for various time points. The samples were resolved and analyzed by the same methods used for the competition EMSA.

### Urea Denaturation Assay

Relative AcrII protein stability was measured by adding urea (denaturation agent) to SpyCas9-sgRNA-dsDNA ternary complexes and quantifying the relative amount of free DNA formation due to dissociation of AcrII by urea addition. The DNA substrate was the same as that used for SpyCas9 cleavage assays. Before addition of radiolabeled DNA, SpyCas9-sgRNA complex (final concentration 100 nM) was purified and diluted in 5X protein binding buffer. Approximate 10 fmol of radiolabeled DNA was added to the reaction mixtures and allowed to form SpyCas9-sgRNA-dsDNA complexes at 22°C for 30 min. Then, serially diluted urea (final concentrations 0, 0.1, 0.25, 0.5, 1, 1.5, 2, 4 M) was added to the ternary complexes and allowed to incubate at 22°C for 30 min. The samples were resolved and analyzed by the same methods used for the competition EMSA.

### Heat Denaturation Assay

Protein thermostability of AcrIIA was measured by heating individual AcrIIA protein at various temperatures (22, 30, 37, 45, 50, 60, 70, 80, 95°C) and measuring their ability to inhibit SpyCas9 cleavage ability. After heating, AcrII proteins (final concentration 50 nM) were cooled down immediately on ice before added to SpyCas9-sgRNA (final concentration 10 nM) reaction mixtures to form ternary complexes. Approximate 10 fmol radiolabeled DNA was then added to each reaction mixture and incubated at 22°C for 30 min. The samples were resolved and analyzed by the same methods used for the DNA cleavage assays.

## DATA AND SOFTWARE AVAILABILITY

### Data Resource

The accession numbers of the 3.4-Å resolution EM map of SpyCas9-sgRNA-AcrIIA2 complex, the 3.9-Å resolution EM map of SpyCas9-sgRNA-AcrIIA2b complex and their corresponding coordinates reported in this paper are EMDB: 9066, 9067; and PDB: 6MCB, 6MCC.

**Molecular Cell, Volume *73***

## Supplemental Information

# Temperature-Responsive Competitive Inhibition of CRISPR-Cas9

**Fuguo Jiang, Jun-Jie Liu, Beatriz A. Osuna, Michael Xu, Joel D. Berry, Benjamin J. Rauch, Eva Nogales, Joseph Bondy-Denomy, and Jennifer A. Doudna**

| SpyCas9 domain | | AcrIIA2 | Interaction pattern§ |
|---|---|---|---|
| REC (Hel-I) | Lys374 | Glu26 | Salt bridge/H-bond* |
| REC (Hel-II) | Asp261 | His15 | H-bond |
| | | Asn19 | H-bond |
| | Lys263 | Phe24 | H-bond |
| | Gln265 | Thr28 | H-bond* |
| NUC (CTD) | **Glu1108** | His37 | H-bond* |
| | | Asp38 | H-bond |
| | **Ser1109** | Asp38 | H-bond* |
| | Ser1136 | Asp96 | H-bond* |
| | **Arg1333** | Ser56 | H-bond |
| | | Asp71 | Salt bridge/H-bond* |
| | **Arg1335** | Ser56 | H-bond |
| | | Ser58 | H-bond* |
| | | Asp71 | Salt bridge/H-bond* |
| | | Thr94 | H-bond* |
| | | Asn95 | H-bond |
| | Ser1338 | Asp60 | H-bond* |

| SpyCas9 domain | | AcrIIA2b | Interaction pattern§ |
|---|---|---|---|
| REC (Hel-I) | Glu371 | Thr74 | H-bond* |
| | Lys374 | Phe75 | Hydrophobic interaction* |
| | | Thr83 | H-bond* |
| NUC (CTD) | **Lys1107** | Asp36 | H-bond* |
| | **Glu1108** | | |
| | Lys1289 | Tyr64 | H-bond* |
| | Gly1218 | Ser95 | H-bond* |
| | **Arg1333** | Thr54 | H-bond |
| | | Asp67 | Salt bridge/H-bond* |
| | | Tyr39 | H-bond* |
| | **Arg1335** | Cys53 | Van der waals |
| | | Thr54 | H-bond |
| | | Ser55 | H-bond* |
| | | Asp67 | H-bond* |
| | | Glu91 | Salt bridge/H-bond* |
| | | Phe94 | Hydrophobic* |
| | Thr1337 | Asn56 | H-bond* |
| | Ser1338 | | |

| SpyCas9 domain | | AcrIIA4 | Interaction pattern[§] |
|---|---|---|---|
| NUC (Linker 1) | Glu766 | Thr22 | H-bond* |
| | Asn767 | Thr22 | H-bond* |
| | | Asp23 | H-bond* |
| NUC (RuvC-III) | Arg973 | Ser26 | H-bond* |
| | His983 | Asn25 | H-bond* |
| NUC (CTD) | **Glu1108** | Asp14 | H-bond |
| | **Ser1109** | | |
| | Ser1136 | Asn35 | H-bond* |
| | | Asn36 | H-bond* |
| | Thr1138 | Asn36 | H-bond* |
| | Ser1216 | Gly38 | H-bond |
| | | Asp37 | H-bond* |
| | Gly1218 | Asp37 | H-bond* |
| | His1311 | Ser46 | H-bond* |
| | | Asn48 | H-bond* |
| | **Arg1333** | Glu40 | H-bond |
| | | Tyr41 | Van der waals forces* |
| | | Glu70 | Salt bridge/H-bond* |
| | | Tyr67 | H-bond* |
| | **Arg1335** | Tyr67 | H-bond/Hydrophobic* |
| | | Asn39 | Salt bridge/H-bond* |

**Table S1. Related to Figures 2 and 5. Summary of the interacting pairs between SpyCas9 and anti-CRISPR proteins (AcrIIA2, AcrIIA2b, and AcrIIA4).**

[§] Salt bridge interaction is defined as the distance between the nitrogen and oxygen atoms is less than 4.0 Å; a hydrogen bond (H-bond) is defined as the distance between the donor and receptor atoms is less than 3.5 Å. * denotes the Acr side chain interactions with Cas9. The residues responsible for PAM recognition (R1333 and R1335) and unwinding at +1 phosphate on the target strand (S1106-S1109) based on crystal structure of Cas9 bound to PAM-containing partial DNA duplex (PDB ID 4UN3), are highlighted in black boldface.

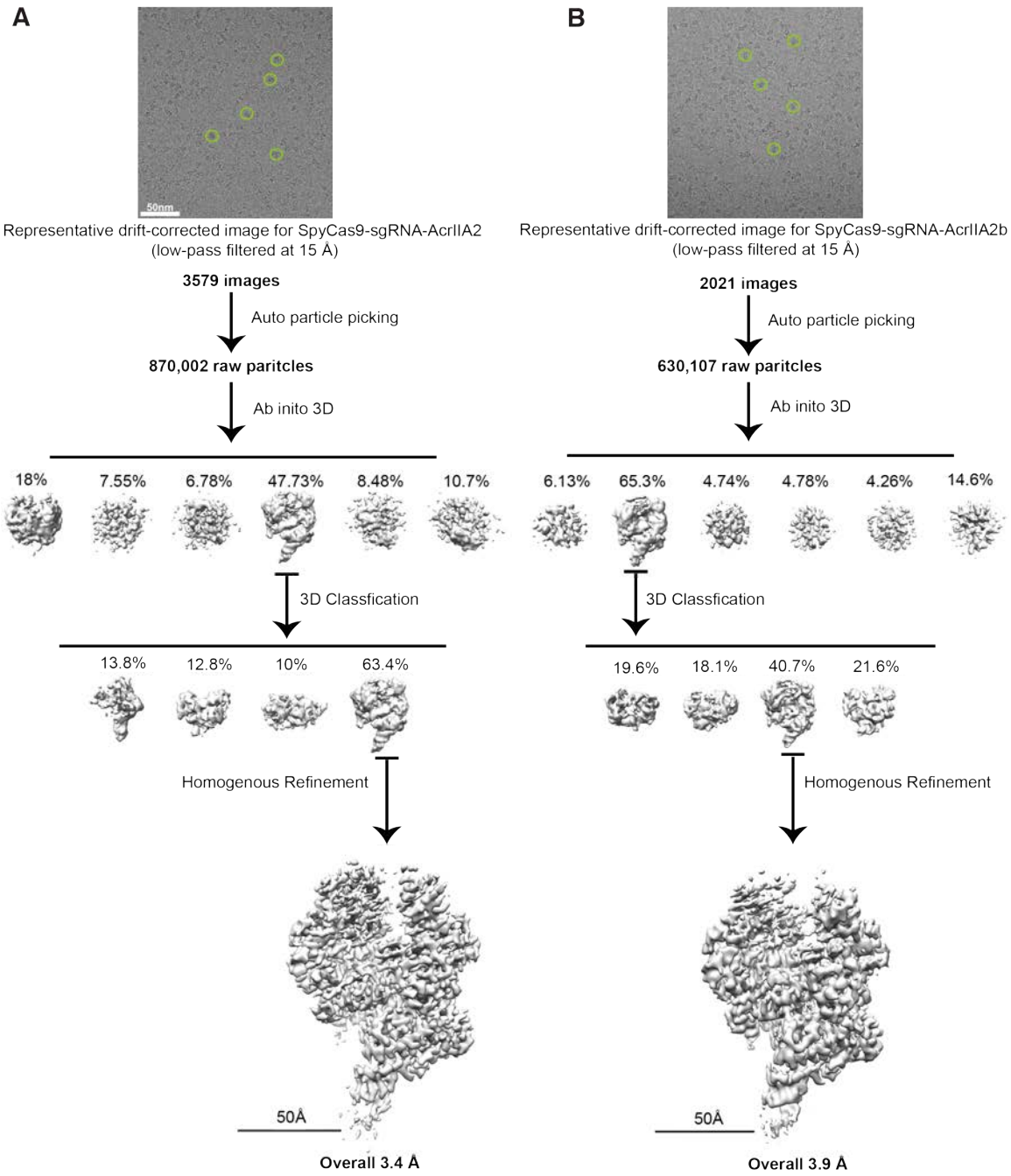


**Figure S1. Related to Figures 2 and 5. Cryo-EM working flow.**

(**A**) For SpyCas9–sgRNA–AcrIIA2 sample, 3579 micrographs were recorded in total. With the templates generated by manually picked particles, we picked 870,002 particles in Gautomatch. All the particles were imported into CryoSPARC and 3D classified into 6 classes via *ab initial* modeling function. The class 4 with 47.7% particles was further selected and 3D classified into 4 classes. The class 4 with 63.4% particles was then refined with a reported resolution of 3.4 Å. (**B**) For SpyCas9-gRNA-AcrIIA2b sample, 2021 micrographs were recorded in total. 630,107 particles picked in Gautomatch were then imported into CryoSPARC and 3D classified into 6 classes via *ab initial* modeling function. The class 2 with 65.3% particles was further selected and 3D classified into 4

classes. The class 3 with 40.7% particles was then refined with a reported resolution of 3.83 Å.

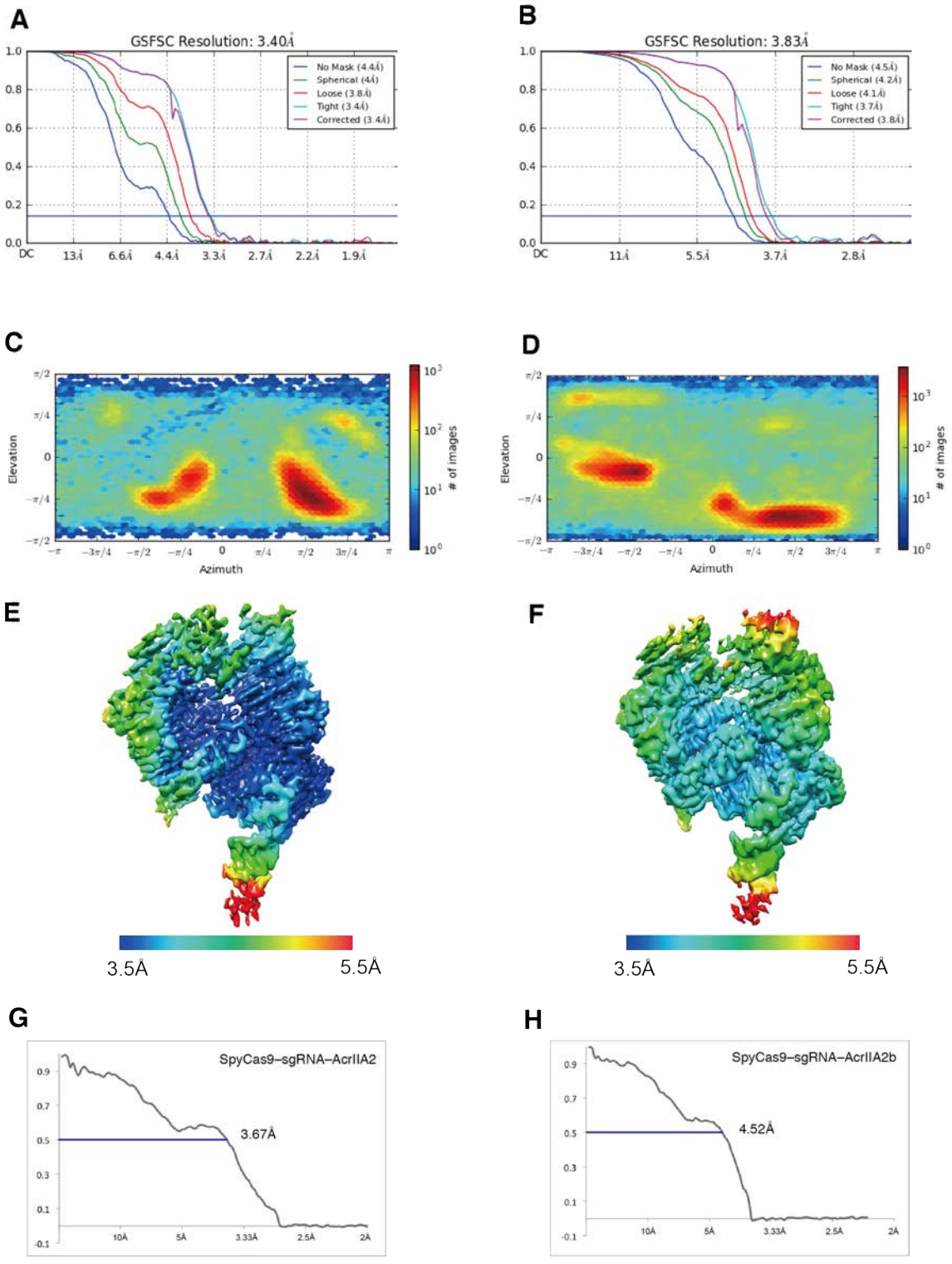


**Figure S2. Related to Figures 2 and 5. EM map and model validation.**
(**A, B**) The Fourier shell correlation (FSC) curves calculated using two independent half maps, indicating an overall resolution of 3.40Å for SpyCas9–sgRNA–AcrIIA2 and 3.84Å for SpyCas9–sgRNA–AcrIIA2b. The panels are the standard output from CryoSPARC.

(**C, D**) The Euler angle distributions of SpyCas9–sgRNA–AcrIIA2 and SpyCas9–sgRNA–AcrIIA2b date sets. These panels are the standard output from CryoSPARC.
(**E, F**) EM structures of the SpyCas9–sgRNA–AcrIIA2 and SpyCas9–sgRNA–AcrIIA2b used for model building were respectively shown and colored by local resolution calculated in Relion2.0. Resolution ranges from 3.5 Å to 5.5 Å. (**G**) FSC curve of SpyCas9–sgRNA–AcrIIA2 EM map against built model. The resolution at the FSC value of 0.5 is 3.67 Å. (**H**) FSC curve of SpyCas9–sgRNA–AcrIIA2b EM map against built model. The resolution at the FSC value of 0.5 is 4.52 Å.

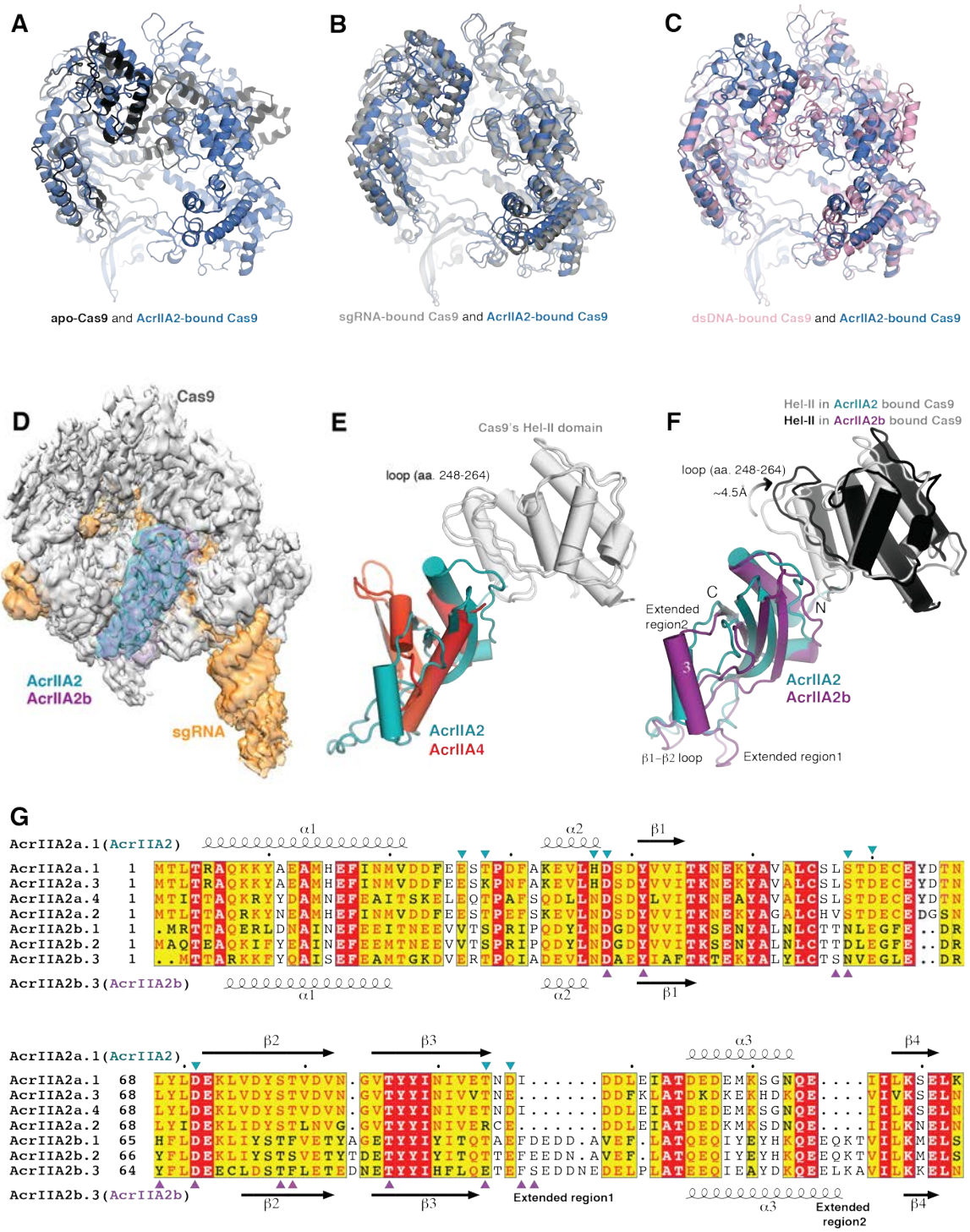


**Figure S3. Related to Figures 2 and 4. AcrIIA2-bound SpyCas9 conformational dynamics and sequence alignment of AcrIIA2 homologs.**

(**A-C**) AcrIIA2-bound SpyCas9 aligned with apo state, sgRNA-bound and DNA-bound state. (**D**) Overlay EM maps of AcrIIA2- and AcrIIA2b-bound SpyCas9 complexes . (**E, F**) Comparison of Helical domain II in AcrIIA2- and AcrIIA2b-bound structures. (**G**) Multiple sequence alignment was carried out by using Clustal Omega (EMBL-EBI), and

illustrated with ESPript. Absolutely conserved residues are shown as white text on a red background. Purple triangles indicate the residues of AcrIIA2b involved in interaction with SpyCas9, whereas the AcrIIA2 residues involved in interacting with SpyCas9 are denoted with teal triangles. The secondary structures of AcrIIA2 and AcrIIA2b are marked on the top and bottom of sequence alignment, respectively.

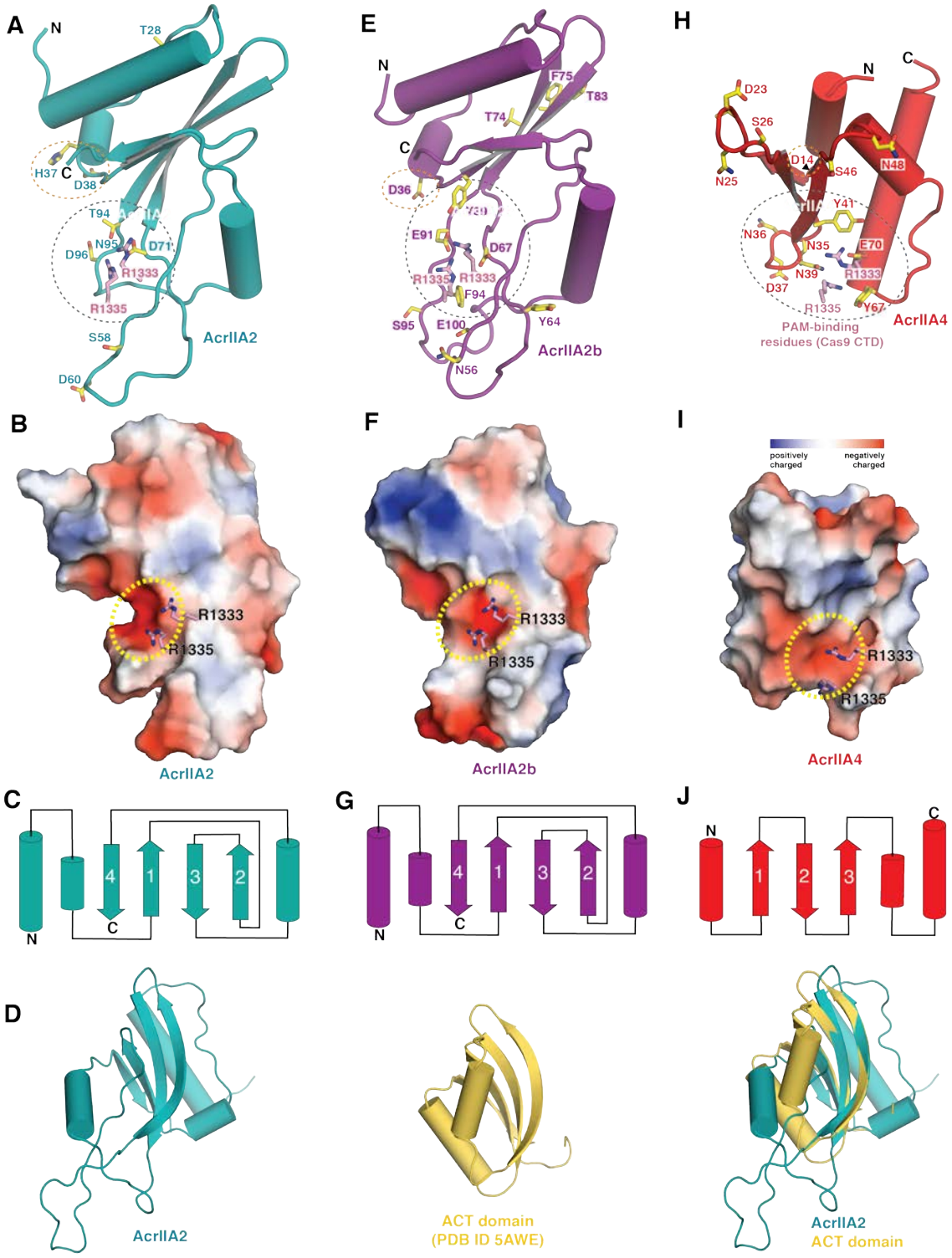


**Figure S4. Related to Figures 2 and 5. AcrIIA2, AcrIIA2b and AcrIIA4 comparison.** (**A, E, H**) Color-labeled residues (and side chains in yellow) to show the critical residues for interaction with SpyCas9 from AcrIIA2a, AcrIIA2b, and AcrIIA4 inhibitor proteins, respectively. (**B, F, I**) Surface electrostatic potential distribution showing PAM recognition residues (R1333/R1335) are buried in an acidic pocket within AcrIIA4, AcrIIA2, and

AcrIIA2b, respectively.. (**C, G, J**) Topology of anti-CRISPRs (AcrIIA2, AcrIIA2b and AcrIIA4). (**D**) A DALI search for structural homologs with a Z score higher than 3.0 showed that AcrIIA2 is structurally similar to aspartate-kinase chorismate-mutase tyrA (ACT) domain (PDB ID 5AWE, Z score = 3.6, RMSD = 3.6 Å, Identity = 14%). The ACT domain, frequently found in a variety of proteins as a regulatory domain, exhibits extremely low sequence identities and high divergence in functionality. Although AcrIIA2 shares a similar β-sheet topology with ACT domain, the flanking helices and the loop regions connecting β strands and α helices are remarkably different.

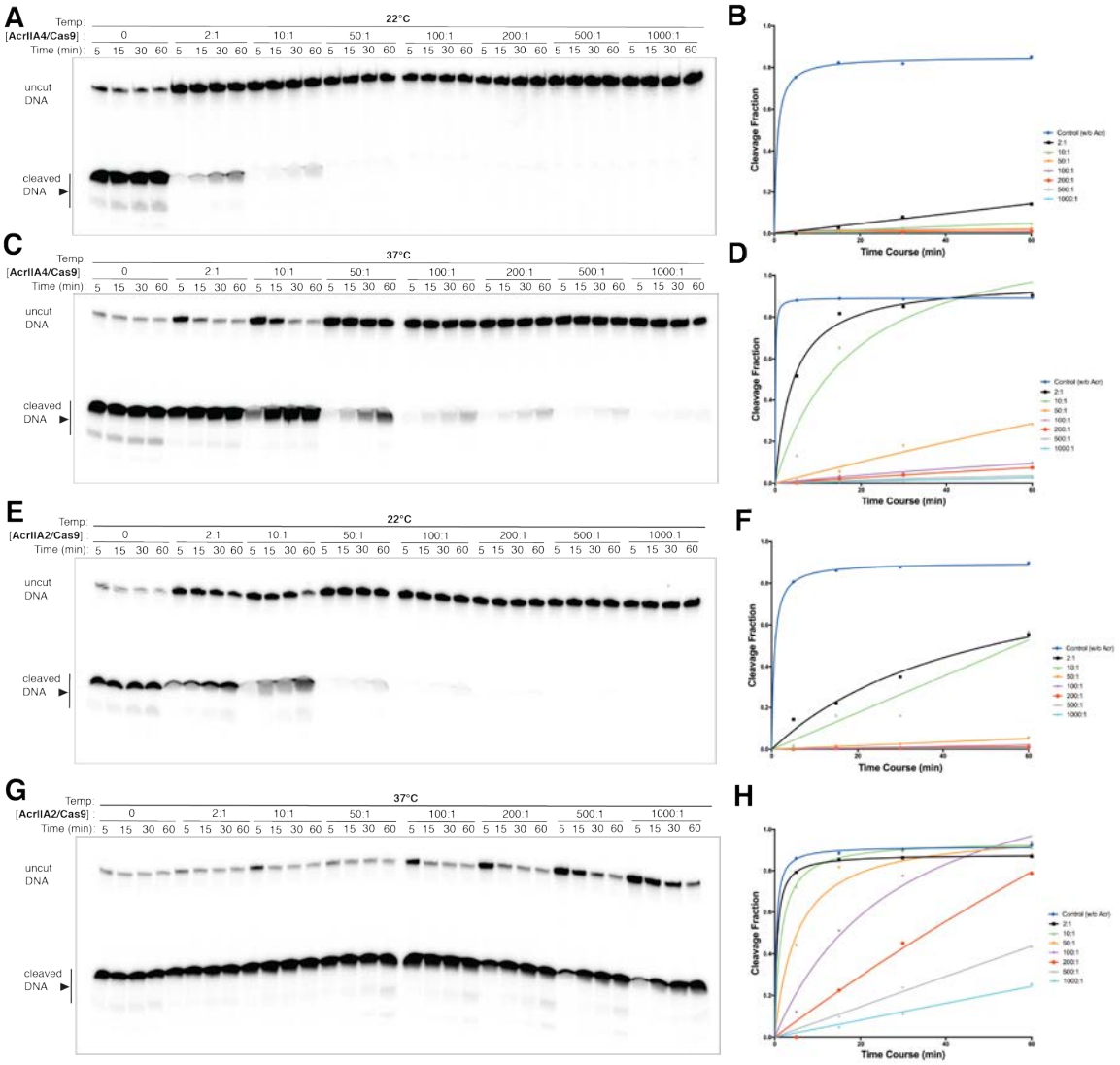


**Figure S5. Related to Figure 3. AcrIIA2 and AcrIIA4 dose-dependent cleavage assays at 22°C and 37°C**

*In vitro* cleavage assays to measure the effect of AcrIIA4/AcrIIA2 dose and incubation time on SpyCas9 activity. AcrII:SpyCas9 molar ratios and incubation times are denoted above each lane. AcrIIA4 and AcrIIA2 both show dose-dependent ability to inhibit SpyCas9 activity. Both show decreased inhibition efficacy at 37°C, but AcrIIA4 is more effective than AcrIIA2 at both 22 and 37°C. (**A, B**) AcrIIA4 and SpyCas9 incubated at 22°C. (**C, D**) AcrIIA4 and SpyCas9 incubated at 37°C. (**E, F**) AcrIIA2 and SpyCas9 incubated at 22°C. (**G, H**) AcrIIA2 and SpyCas9 incubated at 37°C.

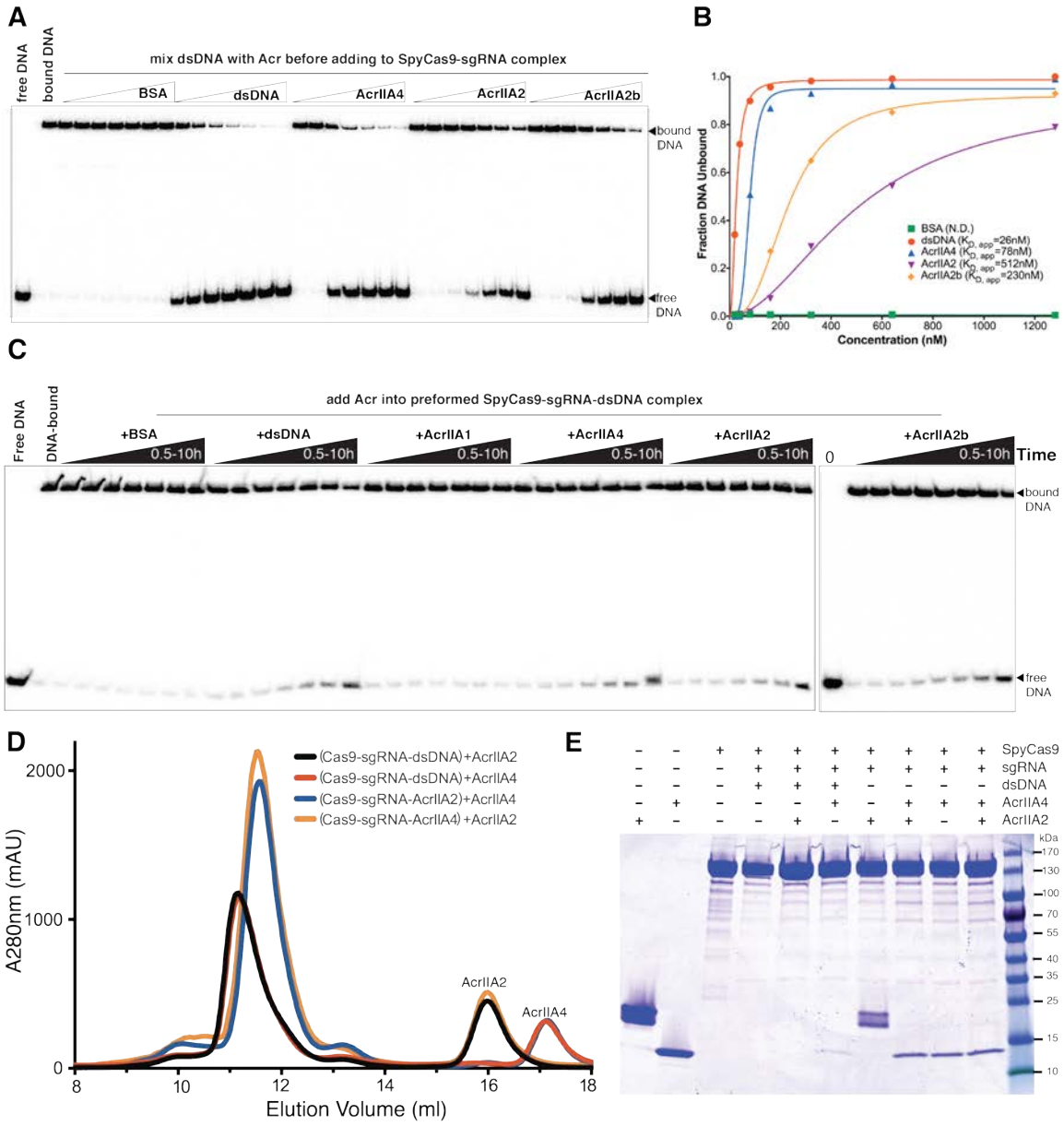


**Figure S6. Related to Figure 3. Competition Assays by EMSA and SEC.**
(**A, B**) SpyCas9-sgRNA was mixed into radiolabeled DNA and cold DNA, AcrIIA4, AcrIIA2, or AcrIIA2b. DNA binds best to SpyCas9, followed by AcrIIA4, AcrIIA2b, and AcrIIA2. (**C**) Preformed SpyCas9–sgRNA–radiolabeled DNA was mixed with cold DNA, AcrIIA1, AcrIIA4, AcrIIA2, or AcrIIA2b and allowed to incubate for 30 min, 1 h, 2 h, 4 h, 6 h, 8 h, or 10 h. The radiolabeled DNA appreciably dissociates from SpyCas9 starting at 4 hours for all samples except BSA and AcrIIA1 (negative control). (**D**) Analytical gel filtration profiles to test whether AcrIIA2 can compete with pre-bound DNA or can compete with pre-bound AcrIIA4. (**E**) SDS-PAGE showing neither anti-CRISPRs can compete with pre-bound DNA, but AcrIIA4 can win out the pre-bound AcrIIA2, but not vice versa.

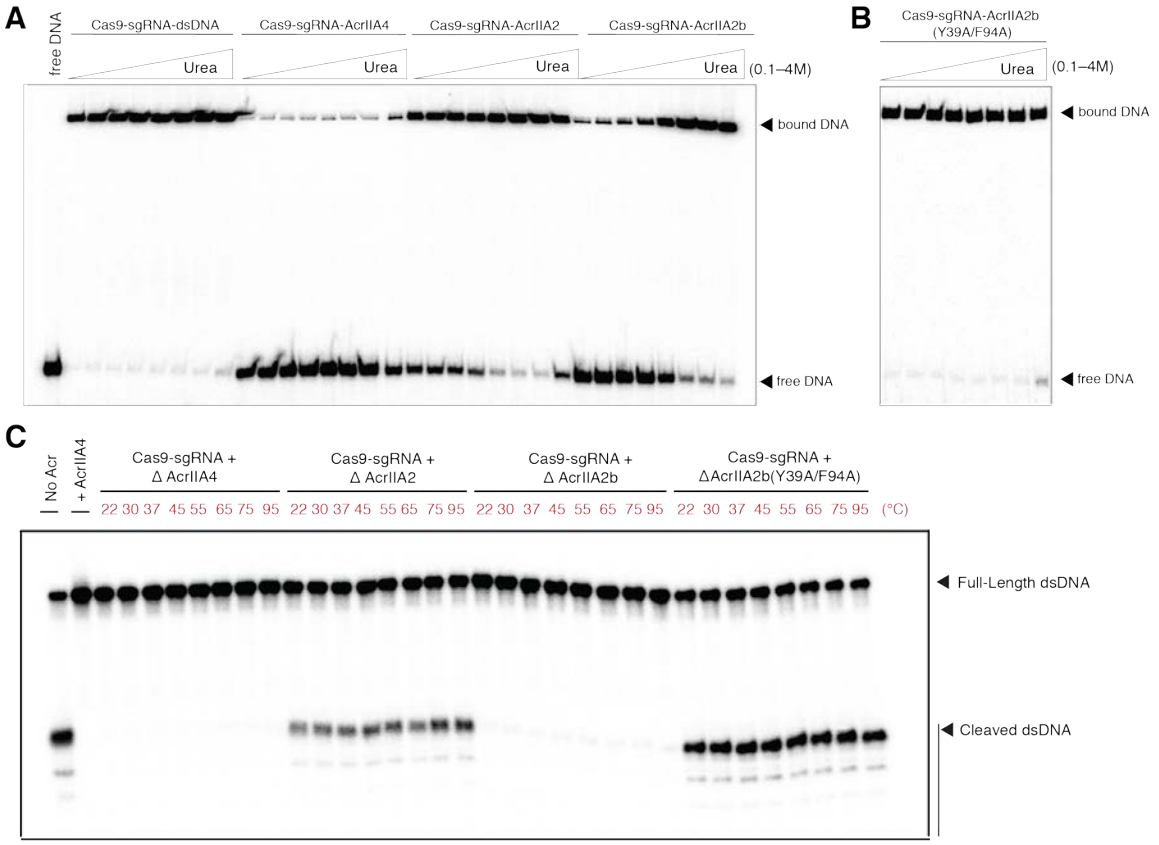


**Figure S7. Related to Figure 5 and 6. AcrIIA2 urea- and heat-induced denaturing assay**

(**A**) *In vitro* gel shift assay to measure stability of AcrIIA4, AcrIIA2, and AcrIIA2b complexed with SpyCas9–sgRNA. AcrIIA4 shows the best stability, as DNA binding is still inhibited at 2-4 M urea. AcrIIA2b is also relatively stable, with significant decay in inhibition efficacy above 1 M urea. AcrIIA2 shows much earlier decay time for inhibition activity. (**B**) AcrIIA2b (Y39A/F94A) shows no inhibition of SpyCas9 binding to DNA regardless of urea concentration. (**C**) *In vitro* cleavage assay to measure whether heat-induced denaturation of AcrIIA4, AcrIIA2, AcrIIA2b, and AcrIIA2b (Y39A/F94A) affect SpyCas9 inhibition efficacy. Aliquots of AcrIIA4, AcrIIA2, and AcrIIA2b were heated at 22, 30, 37, 45, 55, or 65°C for 15 min before cooling down on ice, and then mixed with SpyCas9 at a 10:1 ratio. **Δ** represents preheating Acr at specified temperature and then immediately cold down on the ice before adding into Cas9–sgRNA complex.